

## Structure-property relationships of photofunctional diiridium(II) complexes with tetracationic charge and an unsupported Ir–Ir bond

Fangrui Zheng<sup>1,2,4</sup>, Yuhong Yang<sup>1,4</sup>, Siye Wu<sup>1</sup>, Shunan Zhao<sup>1</sup>, Yifan Zhu <sup>1</sup>, Huimin Su<sup>3</sup>, Jun-Feng Dai<sup>3</sup>, Zeyin Yan<sup>1</sup>, Lung Wa Chung <sup>1</sup>✉ & Keith Man-Chung Wong <sup>1</sup>✉

In contrast to the extensively studied dirhodium(II) complexes and iridium(III) complexes, neutral or dicationic dinuclear iridium(II) complexes with an unsupported ligand are underdeveloped. Here, a series of tetracationic dinuclear iridium(II) complexes, featuring the unsupported Ir(II)–Ir(II) single bond with long bond distances (2.8942(4)–2.9731(4) Å), are synthesized and structurally characterized. Interestingly, compared to the previous unsupported neutral or dicationic diiridium(II) complexes, our DFT and high-level DLPNO-CCSD(T) results found the largest binding energy in these tetracationic complexes even with the long Ir(II)–Ir(II) bond. Our study further reveals that London dispersion interactions enhance the stability cooperatively and significantly to overcome the strong electrostatic repulsion between two half dicationic metal fragments. This class of complexes also exhibit photoluminescence in solution and solid states, which, to our knowledge, represents the first example of this unsupported dinuclear iridium(II) system. In addition, their photoreactivity involving the generation of iridium(II) radical monomer from homolytic cleavage was also explored. The experimental results of photophysical and photochemical behaviours were also correlated with computational studies.

<sup>1</sup>Department of Chemistry, Southern University of Science and Technology, 1088 Xueyuan Blvd., Shenzhen 518055, P.R. China. <sup>2</sup>Analysis and Testing Center, Shenzhen Technology University, 3002 Lantian Road, Shenzhen 518118, P. R. China. <sup>3</sup>Shenzhen Institute for Quantum Science and Engineering, Southern University of Science and Technology, International Quantum Academy (SIQA), and Shenzhen Branch, Hefei National Laboratory, Shenzhen Key Laboratory of Quantum Science and Engineering, Futian District, Shenzhen 518055, China. <sup>4</sup>These authors contributed equally: Fangrui Zheng, Yuhong Yang. ✉email: [oscarchung@sustech.edu.cn](mailto:oscarchung@sustech.edu.cn); [keithwongmc@sustech.edu.cn](mailto:keithwongmc@sustech.edu.cn)

The most common oxidation state of iridium complexes is +3; while those of iridium(II) complexes of  $d^7$  electronic configuration with radical character are rare probably because of their low air- and moisture-stabilities<sup>1–3</sup>. One way to stabilize the iridium(II) complexes is through the formation of a Ir(II)–Ir(II) bond, leading to the pairing up of two individual radicals in the bonding orbital. The Ir(II)–Ir(II) bonds in such dinuclear iridium(II) complexes are usually supported and stabilized by bridging ligands<sup>4–11</sup>. Whereas, diiridium(II) complexes with an unsupported Ir(II)–Ir(II) bond are much less explored and the examples with structurally characterized are even more scarce<sup>12–23</sup>. In all reported complexes, the unsupported iridium(II) metal centres are found to coordinate with anionic ligands leading to the overall formal charge of +2 or 0 (neutral) (Fig. 1). The nature of low formal charge should facilitate the formation of these diiridium(II) complexes with reduced electrostatic repulsion between two half metal fragments. On the other hand, all reported examples with structural characterization were found to exist as only one entity without any derivatives, which precludes systematic study for the understanding of their structure-property relationships, presumably due to challenging synthesis of stable diiridium(II) complexes. In contrast, the isoelectronic dirhodium(II) compounds have been well known and extensively studied for the wide range of applications, such as catalysis<sup>24–33</sup>, antitumor metallopharmaceuticals<sup>34–37</sup>, photo-therapeutic agents<sup>38–40</sup>, photochemistry<sup>41–45</sup> and design of supra-molecular arrays<sup>46–48</sup>.

The photophysical properties of polypyridine or cyclometalated iridium(III) system have also received tremendous attentions. In the past two decades, diversified potential applications<sup>49–52</sup> of the luminescent iridium(III) complexes have been exploited because of their various advantages, such as wide colour-tunability, less thermally accessible  $^3d-d$  state, synthetic versatility and, photo- and chemical-stabilities. In sharp contrast, the photophysical and photochemical studies of unsupported diiridium(II) system are unknown from the limited examples. The exploration and exploitation of such photophysical and photochemical behaviours for the underdeveloped diiridium(II) complexes could open up an avenue for the development of new photofunctional materials. Therefore, synthesis and modification of series of diiridium(II) complexes are crucial and urged for the systematic study.

Herein, we report the synthesis and structural characterization of a series of tetracationic dinuclear iridium(II) complexes,  $[\text{Ir}(\text{II})(\text{N}^{\wedge}\text{N}^{\wedge}\text{N})(\text{CO})(\text{PPh}_3)_2][\text{X}]_4$  (**1–3**) [ $\text{N}^{\wedge}\text{N}^{\wedge}\text{N} = 4,4',4''$ -tri-*tert*-butyl-2,2',6',2''-terpyridine (*t*Bu<sub>3</sub>-terpy), 2,2',6',2''-terpyridine (terpy) and 2,6-bis(*N*-*n*-butylbenzimidazol-2-yl)pyridine (bzimpy)]; X = OTf<sup>−</sup> or BF<sub>4</sub><sup>−</sup>], featuring an unsupported and long Ir(II)–Ir(II) single bond for the first time (Fig. 1). Remarkably, state-of-the-art DFT and DLPNO-CCSD(T) studies revealed that two dicationic Ir(II) fragments are significantly stabilized by considerable London dispersion interactions in these tetracationic diiridium(II) complexes **1–3**. Such non-covalent interactions are responsible for the computed exceptionally largest Ir(II)–Ir(II) binding energy in **1–3**, even though they have a relatively long Ir(II)–Ir(II) bond. It is noteworthy that all of them are found to exhibit photoluminescence in various media, as the first example of the unsupported Ir(II) system. Their electrochemical and photophysical behaviours with different pincer ligands were determined and correlated with the electronic structures obtained from computational studies.

## Results and discussion

**Design and synthesis.** Reaction of  $[\text{IrCl}(\text{PPh}_3)_2(\text{CO})]$  with AgX (X = OTf<sup>−</sup> or BF<sub>4</sub><sup>−</sup>), followed by treatment with the  $\text{N}^{\wedge}\text{N}^{\wedge}\text{N}$  pincer ligand in THF or MeCN at room temperature for 3 days

afforded complexes **1–3** in 52–62% yield (Fig. 2). It is noteworthy that excess Ag(I) ion was added to serve as halide abstraction agent to remove the chloro group in the iridium(I) starting material, and as the oxidizing agent to generate the desired complexes. After addition of the pincer ligand into the pale yellow filtrate from the reaction mixture of  $[\text{IrCl}(\text{PPh}_3)_2(\text{CO})]$  with AgX, greenish black solution was immediately formed. Such dark colour species was identified as  $[\text{Ir}(\text{N}^{\wedge}\text{N}^{\wedge}\text{N})(\text{CO})]^+$ , based on the observation of  $[\text{Ir}(\text{tBu}_3\text{-terpy})(\text{CO})]^+$  at  $m/z = 622.23950$  (calc. for  $[\text{C}_{28}\text{H}_{35}\text{IrN}_3\text{O}]^+$  as 622.24039) in high-resolution mass spectrum (HRMS) during the formation of **1** (Supplementary Fig. S1). Interestingly, upon prolonged stirring, the iridium(I) species was further oxidized to form the desired diiridium(II) complex and red solution with dark red suspension was obtained. Non-covalent Ir(I)–Ir(I)<sup>53,54</sup> and  $\pi-\pi$  interactions are suggested to facilitate the dimerization by holding the molecules into close proximity in the solution. Complexes **1–3** are stable toward air and moisture in the solid state. In dry and degassed CD<sub>3</sub>CN or (CD<sub>3</sub>)<sub>2</sub>SO solution of **1–3**, no observable change from their <sup>1</sup>H NMR spectra was found for at least 24 h. Because of the highly charged nature, their solubilities are good in polar CH<sub>3</sub>CN and DMSO solvents, whereas only slightly to moderately soluble in CHCl<sub>3</sub> and insoluble in toluene. Complexes **1–3** were fully characterized by <sup>1</sup>H, <sup>13</sup>C{<sup>1</sup>H} and <sup>31</sup>P{<sup>1</sup>H} NMR spectrometry, HRMS, IR spectroscopy and satisfactory elemental analysis (Supplementary Figs. S2–S24). <sup>19</sup>F{<sup>1</sup>H} NMR spectrum of **1'** was also recorded to show the signal at  $\delta = -151.16$  ppm for the BF<sub>4</sub><sup>−</sup> anion (Supplementary Fig. S12). The <sup>1</sup>H NMR spectra of **1** and **1'** (Fig. 2) in CD<sub>3</sub>CN at room temperature show broad peaks for the pyridyl signals (Supplementary Figs. S2 and S9), whereas only sharp peaks were observed for those of **2** and **3** under the same conditions (Supplementary Figs. S15 and S20). It is attributable to the restricted rotation between two half units in **1** resulting from the presence of bulky *tert*-butyl groups. These signals can be restored into sharp peaks in other solvents, such as CDCl<sub>3</sub> or (CD<sub>3</sub>)<sub>2</sub>SO (Supplementary Figs. S5 and S6), indicating the freely rotation about the Ir–Ir bond in such media. Their IR spectra show an absorption peak at 2035–2060 cm<sup>−1</sup>, assignable to the  $\nu(\text{C}\equiv\text{O})$  stretching frequency.

**Structure and Bonding.** The molecular structures of **1–3** were determined by X-ray crystallography. Their structural data, selected bond distances and angles are summarized in Supplementary Tables S1–S12. This class of complexes represent the first structural characterized example of tetracationic diiridium(II) system without any bridging ligands. As depicted in Fig. 3a–c, all the complex cations consist of two  $[\text{Ir}(\text{II})(\text{N}^{\wedge}\text{N}^{\wedge}\text{N})(\text{CO})(\text{PPh}_3)_2]^{2+}$  fragments in a head-to-tail arrangement and connected by an unsupported Ir(II)–Ir(II) single bond. Each iridium(II) metal centre is coordinated with one  $\text{N}^{\wedge}\text{N}^{\wedge}\text{N}$  pincer and one CO ligands on the equatorial plane, while the PPh<sub>3</sub> ligand and another iridium(II) metal centre are bound in the axial position to exhibit a distorted octahedral geometry. In all cases, four counter-anions of OTf<sup>−</sup> (or BF<sub>4</sub><sup>−</sup>) are positioned around the corresponding complex cation (Supplementary Fig. S25). It is noteworthy that an interesting structural feature of these complexes is generally the longer Ir(II)–Ir(II) bond distance (**1**, 2.8942(4) Å; **2**, 2.9421(9) Å; **3**, 2.9731(4) Å), compared to the previously reported unsupported neutral or dicationic diiridium(II) complexes (2.66–2.84 Å)<sup>12–23</sup>.

The shortest Ir–Ir bond was observed in **1** even with bulky *tert*-butyl groups, whereas the longest one was found in **3** with the larger  $\pi$ -conjugated pincer ligand of bzimpy. By changing the counter-anion from OTf<sup>−</sup> to BF<sub>4</sub><sup>−</sup> in **1'** as shown in Supplementary Fig. S25, the complex cation exhibited similar structural features with elongation of the Ir–Ir bond (2.9135(5) Å). The

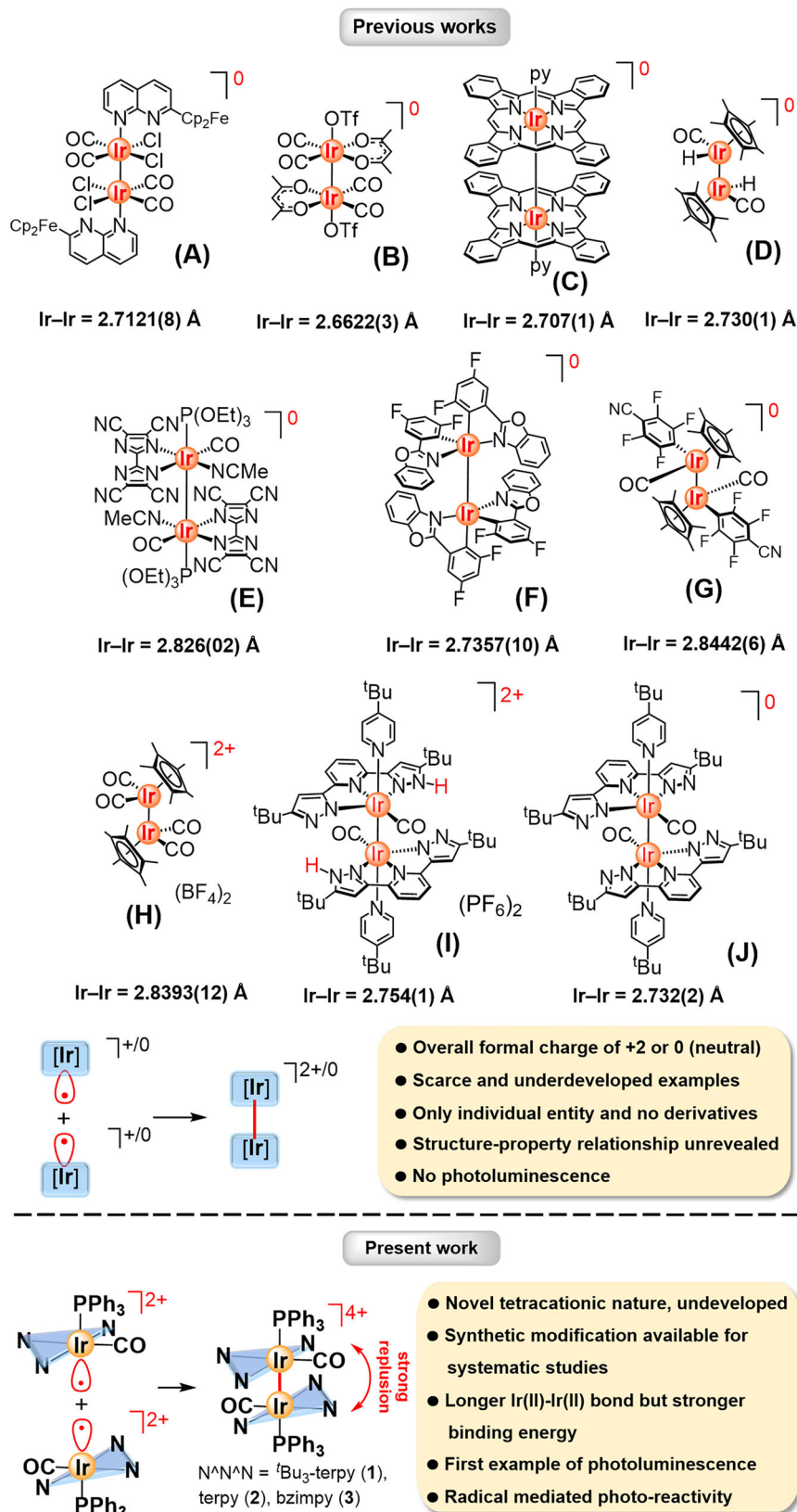


**Fig. 1** Previous examples with neutral or dicationic charge and this work with tetracationic charge. Previous works (A–J). Diiridium(II) complexes with unsupported Ir(II)–Ir(II) bond, formed from two d<sup>7</sup> Ir(II) fragments and the uniqueness of tetracationic diiridium(II) complexes (1–3) in this study.

change in this Ir–Ir bond length is ascribed to the different non-covalent interaction between the complex cation and counter anions in crystal packing. The C≡O bond distances of 1.121(8)–1.135(4) Å are in the typical range of transition metal complexes. In **1**, the peripheral pyridine rings of <sup>t</sup>Bu<sub>3</sub>-terpy are found to tile from the central pyridine group with the interplanar angles of 10.674(67)–13.455(59)°, attributable to the mutual repulsion from bulky *tert*-butyl groups. On the other hand, such deviation from coplanarity in the pincer ligand is diminished in **2** and **3** with the interplanar angles of 4.496(252)–5.383(258)° and 4.430(94)–4.507(102)°, respectively. The interplanar distances between the peripheral rings of pincer ligands on two half units are 3.2050(20)–3.2738(21) Å (**1**), 3.0761(71)–3.1702(77) Å (**2**) and 3.1890(36)–3.1981(37) Å (**3**), indicating the presence of π–π interactions. In addition, two phenyl rings on the axial PPh<sub>3</sub> ligand are arranged in a parallel way to the pincer ligand with small tilted angles and short distances for the better π–π stacking (Fig. 3d–f).

DFT (including M06-L, M06, B3LYP-D3, PBE0-D3 and MN15 methods) and high-level DLPNO-CCSD(T) calculations<sup>55–62</sup>

were performed to examine the unusual tetracationic Ir(II) complexes **1–3** with unsupported long Ir(II)–Ir(II) bond. In addition, three model complexes (**4–6**), other previously reported complexes with unsupported metal–metal bond, including ten Ir(II)–Ir(II), one Rh(II)–Rh(II) and one Au(II)–Au(II) complexes (**A–L**), were also examined for comparison (Fig. 4)<sup>12–23,63,64</sup>. Despite the computed Ir–Ir bonds of **1–3** (2.94–2.99 Å) are generally longer, the present system was surprisingly computed to have a larger binding free energy ( $\Delta G_{\text{soln}}$ : *ca.* –49 kcal/mol by the SMD M06-L//M06-L method), compared to **A–J** ( $\Delta G_{\text{soln}}$ : *ca.* –24 to –39 kcal/mol), **K** ( $\Delta G_{\text{soln}}$ : –44 kcal/mol) and **L** ( $\Delta G_{\text{soln}}$ : –35 kcal/mol), as shown in Fig. 4. Such energetic trend was qualitatively supported by different DFT and high-level DLPNO-CCSD(T) methods (Supplementary Fig. S26 and Supplementary Table S13). It is noteworthy that the diiridium(II) complexes **1–3** were found to have such large binding energies, even though they have smaller electron density ( $\rho$ ) and positive electron density ( $\nabla^2\rho$ ) values<sup>65–69</sup> (Supplementary Table S13). Our computational study clearly manifests that the bonding features (a longer bond distance with a larger binding energy) for the tetracationic complexes **1–3** are unprecedented.

In order to further unravel the bonding features of **1–3**, distortion/interaction analysis<sup>70</sup> was employed and these results showed that the large binding energy is mainly attributed to the considerable interaction energy (Supplementary Fig. S27a). Interestingly, a much larger interaction energy plays the key role of the largest binding energy determined in **1** ( $\Delta E_{\text{int,soln}}$ : *ca.* –91 kcal/mol), relative to **2** and **3** (*ca.* –65 to –68 kcal/mol). While, entropy effect favors **3** > **1**, which reduces their binding free-energy difference. Empirical dispersion (e.g. D3 contribution for B3LYP method) correction<sup>61</sup> (Supplementary Fig. S27b and Supplementary Table S14) and non-covalent interactions (NCIs) analysis<sup>71</sup> further demonstrated that London dispersion (Fig. 5a for **1** and Supplementary Fig. S28a for **2** and **3**), including π–π interactions among the two pincer ligands and the four OTf<sup>–</sup> counterions, play one of the key roles in their high binding energies. These interactions can also be visualized by the bond-critical-points (BCPs) from the results of the quantum theory of atoms in molecules (QTAIM) method<sup>72,73</sup>. (Fig. 5b for **1** and Supplementary Fig. S28b for **2** and **3**). In this connection, a longer Ir–Ir bond distance (3.08 Å) and much smaller binding energy

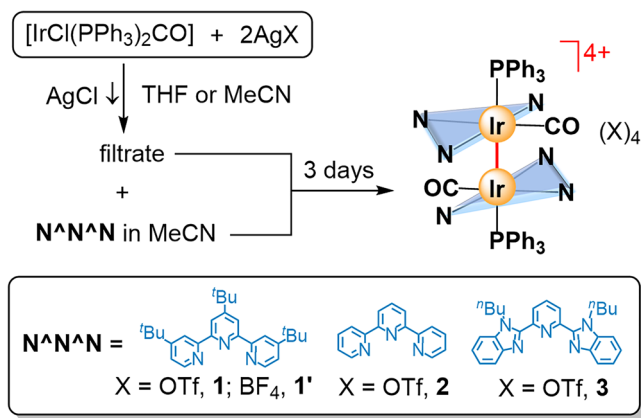


**Fig. 2** Synthetic route of tetracationic diiridium(II) complexes with an unsupported Ir–Ir bond tetracationic diiridium(II) complexes. Synthesis of **1–3** with different pincer ligands.

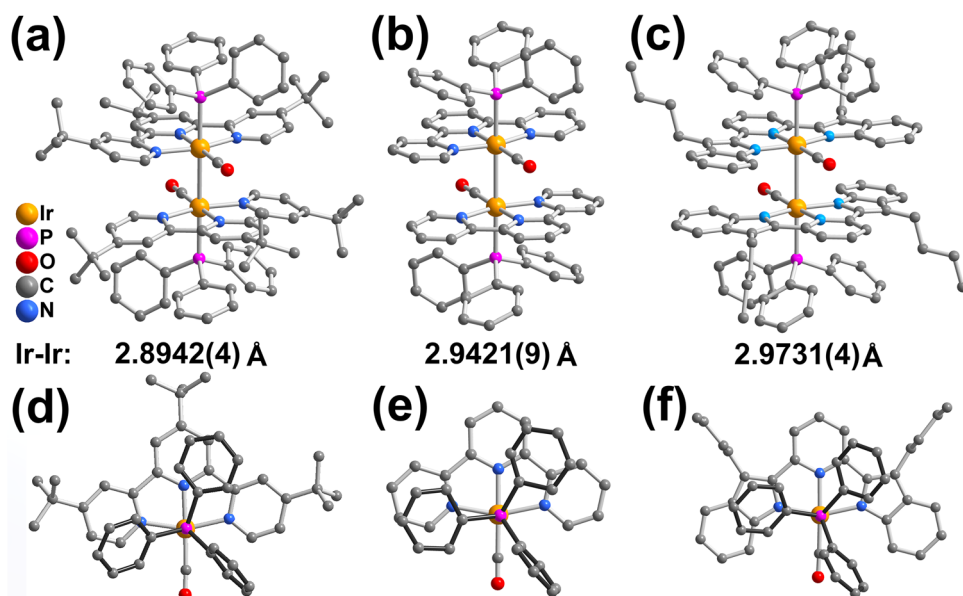


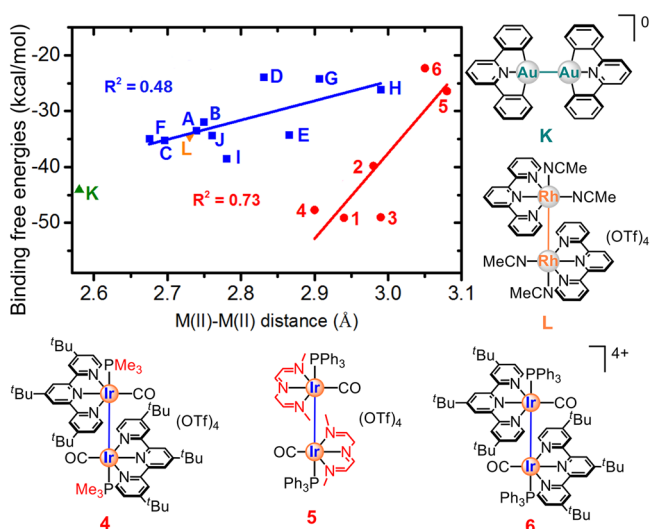
**Fig. 3** X-ray crystal structures of **1–3**. Complex cations of **1–3** (a–c) and their corresponding half fragments from top view (d–f). Hydrogen atoms and solvent molecules are omitted for clarity.

( $\Delta G_{\text{soln}}$ : ca.  $-26.4$  kcal/mol) were also computed for model complex **5**, in which a smaller and less conjugated tridentate pincer ligand with smaller dispersion stabilization was adopted. This result is in agreement with other previous computational studies suggesting the importance of London dispersion in some metal complexes<sup>74–81</sup>. As shown in Supplementary Table S14, both metal–metal<sup>82</sup> and non-covalent interactions among the tridentate pincer ligands and counterions should be generally the critical factors in stabilizing the rare Ir(II)–Ir(II) bond and rendering the unusually large binding energies for tetracationic complexes **1–3** by conquering unfavorable and strong electrostatic repulsions.

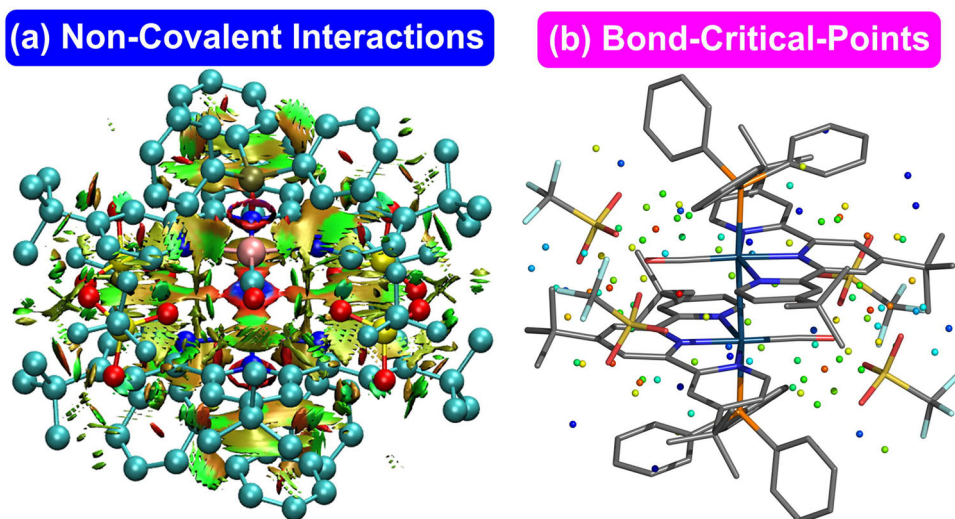
**Photophysical and electrochemical behaviours.** The photophysical and electrochemical behaviours of **1–3** have been investigated and the data are summarized in Table 1. Their UV-vis absorption spectra of **1–3** in  $\text{CH}_3\text{CN}$  are also depicted in

Fig. 6. In addition to the intraligand (IL)  $\pi$ – $\pi^*$  absorptions of  $\text{N}^{\wedge}\text{N}^{\wedge}\text{N}$  pincer ligand at 343 and 385 nm, the UV-Vis absorption spectra exhibit a low-energy absorption band at 493–553 nm. Our TD-DFT (CPCM TD-B3LYP-D3//M06-L) calculations<sup>18</sup> suggested that the low-energy absorption is mainly ascribed to metal–metal bond-to-ligand charge transfer (MMLCT)  $d\pi(\text{Ir}–\text{Ir}) \rightarrow \pi^*(\text{N}^{\wedge}\text{N}^{\wedge}\text{N} \text{ ligand})$  transition with some mixing of  $d\pi(\text{Ir}–\text{Ir}) \rightarrow d\pi^*(\text{Ir}–\text{Ir})$  character (Supplementary Figs. S29–S31). Such an assignment is also consistent with the computed composition of the donor/highest occupied molecular orbital (Ir–Ir, 31–37%; P, 18–23%;  $\text{N}^{\wedge}\text{N}^{\wedge}\text{N}$  ligand, 15–18%) and the acceptor/lowest unoccupied orbital (Ir–Ir, 13–18%; P, 1–2%;  $\text{N}^{\wedge}\text{N}^{\wedge}\text{N}$  ligand, 62–80%) for **1–3** by the M06-L method (Table 2). Figure 5a also shows the schematic frontier molecular orbital (FMO) diagram of the ground-state metal complexes, illustrating the key MOs involved in the lowest-lying electronic transition of the MMLCT character. Interestingly, this absorption band in **1** with electron-rich *tert*-butyl groups exhibited a slight red-shift, relative to **2**. The change in the pincer ligand was found to vary the energy levels of HOMO and LUMO at the same time, as revealed from the potentials for the first oxidation and reduction (vide infra). In view of this, the MMLCT absorption energy could not simply correlate to the  $\pi^*$  orbital energy level by subtle modification in the pincer ligand. For complex **3** with substantial lower-lying  $\pi^*$  orbital in bzimpy ligand, this absorption band was found to shift to lower energy significantly. Despite of this, our TD-DFT calculations also suggested the red-shift absorption trend of the two key low-lying transitions from **1** to **3** (**1**: 377 and 496 nm; **3**: 398 and 540 nm; Supplementary Tables S15–S17). This result further supports the assignment of such low-energy absorption band as MMLCT transition based on the substantial lower-lying  $\pi^*$  orbital energy level of bzimpy ligand in **3** (540 nm), relative to **1** (496 nm) with terpyridine ligand.

Upon excitation at  $\lambda_{\text{ex}} > 450$  nm on their MMLCT absorption bands, **1–3** were found to exhibit orange-red luminescence at 620–678 nm in degassed  $\text{CH}_3\text{CN}$  solution at 298 K (Fig. 6). To the best of our knowledge, this is the first example of unsupported diiridium(II) systems showing luminescence. Their excitation bands from the excitation spectra in degassed  $\text{CH}_3\text{CN}$  solution were found to resemble to the corresponding low-energy absorption bands (Supplementary Fig. S32). In addition, the luminescence intensity of **1** diminishes to around 50% as in aerated  $\text{CH}_3\text{CN}$  solution. Collectively, together with the large



**Fig. 4** Correlation of the computed M(II)–M(II) bond distances and binding free energies. The plot of metal(II)–metal(II) distances (Å) and their relative binding free energies (in kcal/mol) for some unsupported metal(II)–metal(II) complexes (M: Ir, Rh or Au) in acetonitrile by the SMD M06-L//M06-L method.



**Fig. 5** Non-covalent interactions of **1**. **a** Non-covalent interactions (NCIs) analysis (red: strong repulsion; green: weak attraction; blue: strong attraction) and **b** the QTAIM analysis (Bond-Critical-Points (BCPs) in a sphere form; red: highest  $\rho$ ; blue lowest  $\rho$ ) in **1** based on the SMD M06-L//M06-L methods.

**Table 1** Photophysical and electrochemical data of 1-3.

	Absorption <sup>a</sup> $\lambda_{\text{abs}}$ , nm ( $\epsilon$ , $10^4 \text{ dm}^3 \text{ mol}^{-1} \text{ cm}^{-1}$ )	Medium	Emission $\lambda_{\text{emr}}$ , nm ( $\tau$ , ps)	Emission quantum yield $\Phi_{\text{lum}}$	Ox. <sup>b</sup> $E_{\text{pa}}$ <sup>c</sup> , V vs. SCE	Red. <sup>b</sup> $E_{\text{pc}}$ <sup>d</sup> , V vs. SCE
<b>1</b>	343 (3.29), 385 (3.52), 502 (1.52)	CH <sub>3</sub> CN <sup>e</sup> (298 K)	620 (63; 294)	$4.99 \times 10^{-4}$	+1.80	-0.4
		solid (298 K)	653 (90; 360)	$\frac{f}{-}$		
		solid (77 K)	624	$\frac{f}{-}$		
<b>2</b>	352 (2.37), 375 (2.89), 494 (0.89)	CH <sub>3</sub> CN <sup>e</sup> (298 K)	650 (55; 359)	$2.62 \times 10^{-4}$	+1.90	-0.30
		solid (298 K)	632 (135)	$\frac{f}{-}$		
		solid (77 K)	610	$\frac{f}{-}$		
<b>3</b>	343 (8.47), 394 (12.90), 513 (2.07), 551 (2.89)	CH <sub>3</sub> CN <sup>e</sup> (298 K)	678 (55; 292)	$0.85 \times 10^{-4}$	+1.73	-0.26
		solid (298 K)	673 (68; 396)	$\frac{f}{-}$		
		solid (77 K)	647	$\frac{f}{-}$		

<sup>a</sup> In acetonitrile. <sup>b</sup> In acetonitrile solution with <sup>n</sup>Bu<sub>4</sub>NPF<sub>6</sub> (0.1 M) as the supporting electrolyte at room temperature; scan rate 100 mV s<sup>-1</sup>. <sup>c</sup>  $E_{\text{pa}}$  refers to the anodic peak potential for the irreversible oxidation waves. <sup>d</sup>  $E_{\text{pc}}$  refers to the cathodic peak potentials for irreversible reduction waves. <sup>e</sup> In degassed solution at 298 K. <sup>f</sup> Not determined.

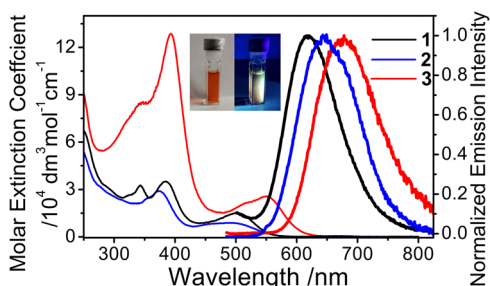


**Fig. 6** Photophysical studies of 1-3 in solution state. UV-vis absorption (thin line) and emission (thick line) spectra of complexes 1-3 in CH<sub>3</sub>CN solution at 298 K. Excitation at  $\lambda_{\text{ex}} = 470$  nm. Inset shows the photographs of 1 in degassed CH<sub>3</sub>CN solution under ambient light and UV light.

Stokes shift, such luminescence of 1-3 is assigned to be originated from the triplet metal-metal bond-to-ligand charge transfer (<sup>3</sup>MMLCT), with some mixing of  $d\pi(\text{Ir}-\text{Ir}) \rightarrow d\pi^*(\text{Ir}-\text{Ir})$  character, as shown in Fig. 7b. This assignment is also qualitatively consistent with the spin density of the optimized triplet structure and emission transition for <sup>3</sup>1 by the M06-L and TD-B3LYP-D3//M06-L methods, respectively (Supplementary Figs. S33-S36). Similar to the low-energy absorption bands, the luminescence energy of 3 (678 nm) is lower than those of 1 (620 nm) and 2 (650 nm), which further supports the nature of <sup>3</sup>MMLCT origin. Qualitatively, our CPCM TD-B3LYP-D3//M06-L (including effect of spin-orbital coupling) calculations<sup>83-85</sup> also supported the observed red-shift luminescence of 3 for the assignment of <sup>3</sup>MMLCT excited state (1: ~611 nm vs. 3: ~644 nm; Supplementary Tables S18-S20). It is noteworthy that the UV-vis absorption and luminescence spectra of <sup>3</sup>1' (Supplementary Fig. S37) with the counter anion of BF<sub>4</sub><sup>-</sup> showed essentially the same spectra as in 1, indicative of insignificant influence from its counter anion in the solution state.

The luminescence quantum yield ( $\Phi_{\text{lum}}$ ) of 1-3 (1,  $4.99 \times 10^{-4}$ ; 1',  $4.86 \times 10^{-4}$ ; 2,  $2.62 \times 10^{-4}$ ; 3,  $0.85 \times 10^{-4}$ ) were obtained in degassed CH<sub>3</sub>CN. The decrease in  $\Phi_{\text{lum}}$  from 1 to 3 with lower luminescence energy is probably due to the effect arising from the energy gap law. It is noteworthy that very short luminescence lifetimes ( $\tau_1 = 55-63$  ps;  $\tau_2 = 291-389$  ps) were revealed in degassed CH<sub>3</sub>CN or in solid state 298 K (Table 2 and Supplementary Figs. S38-S39). Such short luminescence lifetime and low  $\Phi_{\text{lum}}$  could be realized by intersystem crossing back to the ground state from the triplet-state minimum, which could facilitate non-radiative decay pathway with a low-energy barrier at their minimum crossing point (MECP)<sup>86</sup> as suggested from our DFT calculations for 1 (Supplementary Fig. S40). In addition,

**Table 2** Composition of donor and acceptor molecular orbitals of 1-3 in gas phase by the M06-L method.

	MO	Ir, %	P, %	Pincer, %
<b>1</b>	Acceptor (LUMO)	18	2	62
	Donor (HOMO)	37	23	17
<b>2</b>	Acceptor (LUMO)	15	1	76
	Donor (HOMO)	31	19	15
<b>3</b>	Acceptor (LUMO)	13	1	80
	Donor (HOMO-2)	31	18	18

photogeneration of radical monomer as a competing process is also responsible for the rapid deactivation process for the <sup>3</sup>MMLCT excited state (vide infra). On the other hand, 1-3 were also found to exhibit photoluminescence at 632-673 nm in the solid state at 298 K (Supplementary Fig. S41a), while the corresponding luminescence at 77 K showed a blue-shift energy at 610-648 nm with narrower band shape (Supplementary Fig. S41b). It is interesting to note that the emission energies of 1' in solid state at room temperature and 77 K are found to be higher than those of 1 (Supplementary Fig. S42). This could be rationalized by the lower-lying HOMO in 1' resulting from the longer Ir-Ir bond, which was observed from their crystal structures. Since the LUMOs of 1 and 1' are predominantly of  $\pi^*$  orbital of the same terpyridine ligand, larger HOMO-LUMO energy gap in 1' could give rise to higher emission energy in solid state.

The electrochemical behaviours of 1-3 were also studied by cyclic voltammetry in CH<sub>3</sub>CN (0.1 M <sup>n</sup>Bu<sub>4</sub>NPF<sub>6</sub>) at 298 K (Table 1 and Supplementary Fig. S43). The oxidative scan showed an irreversible anodic wave (1, +1.80 V; 2, +1.90 V; 3, +1.73 V) (vs. SCE), attributed to the Ir(II) metal centre oxidation with some mixing of PPh<sub>3</sub> ligand. The less positive potential for this oxidation in 1, relative to 2, is ascribed to the more electron-rich Ir(II) metal centre, through the incorporation of terpyridine ligand with electron-donating *tert*-butyl groups. Upon reductive scan, an irreversible cathodic wave at -0.26 V to -0.40 V (vs. SCE) was observed, which is reasonably assigned as the reduction on the terpyridine ligand with some  $\pi^*(\text{Ir(II)}-\text{Ir(II)})$  character. The reduction potentials of these cathodic waves (1, -0.26 V; 2, -0.30 V; 3, -0.40 V) are in agreement with the  $\pi^*$  orbital energy level of the pincer ligand. Compared to 1 and 2, the smallest potential difference between the potentials for oxidation and reduction in 3 is well correlated with the observation of the smallest MMLCT absorption energy. The essentially irreversible nature of this reduction process is probably due to dissociation of

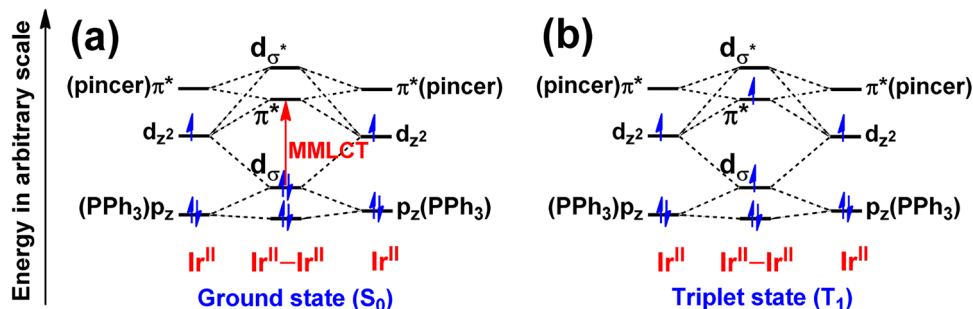


**Fig. 7** Illustration of the origin and Ir-Ir bond weakening in triplet excited state. Schematic frontier molecular orbital (FMO) diagrams of **1-3** in the ground (a) and the lowest-lying triplet (b) states. Note that the relative energy is an arbitrary value. Only the key orbitals with main contribution are shown.

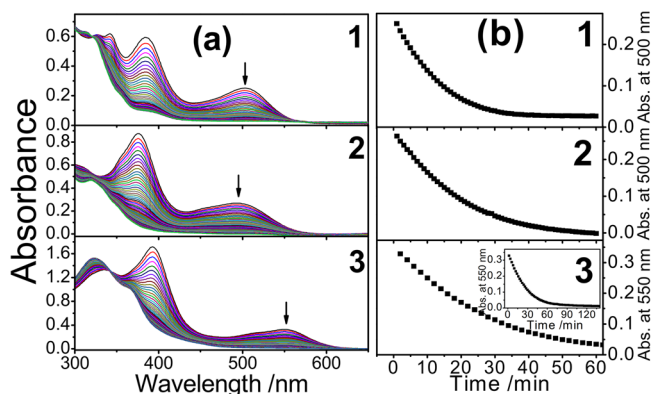


**Fig. 8** Photostability studies of **1-3**. **a** UV-vis spectral changes of **1-3** in  $\text{CH}_3\text{CN}$  solution at 298 K upon irradiation at 500 nm. **b** The plot of absorbance versus time for **1** and **2** (1-min time interval), and **3** (2-min time interval).

the diiridium(II) framework, resulting from the population of  $\pi^*(\text{Ir}(\text{II})-\text{Ir}(\text{II}))$  orbital. In **1**, an additional anodic peak at  $-0.16$  V is only emerged after the first reduction scan beyond  $-0.40$  V (Supplementary Fig. S43a), indicative of the oxidation of the decomposed product. Similar to the photophysical properties, the observation of almost the same reduction potentials for the reduction and oxidation of **1'** (Supplementary Fig. S44) and **1**, indicated the insignificant effect from the change of counter anion in solution state.

**Photoreactivity.** In connection with the unprecedentedly high binding energy by our DFT calculations, **1-3** were found to be inert towards  $\text{O}_2$ ,  $\text{H}_2\text{O}$ , as well as  $\text{Br}_2$  and  $\text{I}_2$  in  $\text{CH}_3\text{CN}$  solution. In view of the corresponding bonding(Ir-Ir) and anti-bonding(Ir-Ir) characters in their donor and acceptor orbitals (Fig. 7), the Ir-Ir bond cleavage resulting from photoexcitation would be anticipated to generate the respective radical monomer  $[\text{Ir}(\text{N}^{\wedge}\text{N}^{\wedge}\text{N})(\text{CO})(\text{PPh}_3)]^{2+\bullet}$ . As shown in Fig. 8, such photoreactivity behaviour was realized by the UV-vis spectral changes of **1-3** in  $\text{CH}_3\text{CN}$  solution upon photoirradiation at the region of the MMLCT absorption band (Fig. 8a). By keeping the absorbance of **1-3** the same at 500 nm for the photoirradiation, the absorbance changes with time were monitored and their relative photostabilities could be qualified as  $1 < 2 < 3$  (Fig. 8b). The higher photostability would be envisioned for the complex with the computed smaller contribution from Ir(II) metal centre for the donor and acceptor orbitals (Table 2), which is in line with the experimental results of their relative photostabilities. The vanishment of the MMLCT absorption bands suggests that the photogenerated radical monomers would repel from each other to avoid the radical-radical coupling for the backward formation of

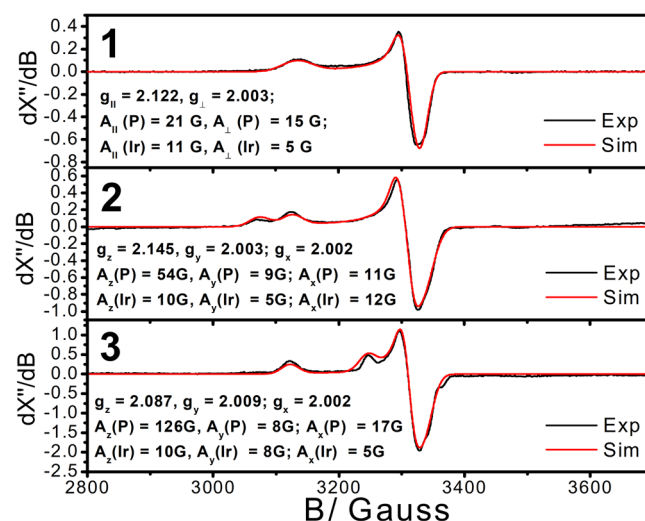


**Fig. 9** X-Band EPR spectra of **1-3**. The spectra were recorded for the samples in  $\text{CH}_3\text{CN}$  at 100 K after white light photoirradiation for 5 min at 298 K (black) and the simulated spectra (red). Frequency: 9.299527 GHz; modulation amplitude: 8.0 G; power: 2.0 mW.

the diiridium(II) complex. The photostability of **1'** was also found to be similar to that of **1**, suggesting that the influence of counter anion is insignificant in the solution state.

Electron paramagnetic resonance (EPR) spectroscopy is a suitable technique to probe the formation of radical monomer upon photoirradiation. The EPR spectra of **1-3** in  $\text{CH}_3\text{CN}$  at 100 K after photoirradiation for 5 min in solution state are depicted in Fig. 9. The EPR spectra clearly indicate that the photogenerated species are of  $S = 1/2$  paramagnetic nature with typical axial symmetry<sup>87,88</sup>. On the basis of the  $g$ -tensor values ( $g_z > g_x, g_y > 2$ ) suggestive of a compressed octahedral structure<sup>88</sup>,  $[\text{Ir}(\text{N}^{\wedge}\text{N}^{\wedge}\text{N})(\text{CO})(\text{PPh}_3)(\text{CH}_3\text{CN})]^{2+\bullet}$  species is likely generated arising from readily occupation of the vacant site in 5-coordinated  $[\text{Ir}(\text{N}^{\wedge}\text{N}^{\wedge}\text{N})(\text{CO})(\text{PPh}_3)]^{2+\bullet}$  by a  $\text{CH}_3\text{CN}$  solvent molecule. It is noteworthy that no corresponding EPR signal would be observed for **1-3** in the absence of photoirradiation, which further supports the formation of radical being originated from the photocleavage process.

According to the isolobal analogy, the  $d^7$  five-coordinate  $[1_{1/2}]^{2+\bullet}$  species upon photocleavage is isolobal to  $\text{CH}_3^{\bullet}$  radical with similar reactivity towards  $\text{Br}_2$  or  $\text{I}_2$  (Fig. 10a). Interestingly, mononuclear iridium(III) complexes,  $[\text{Ir}(\text{Bu}_3\text{-terpy})(\text{CO})(\text{PPh}_3)\text{X}]^{2+}$  [ $\text{X} = \text{Br}$ , **7** (yield = 83%);  $\text{I}$ , **8** (yield = 78%)] were afforded from the reactions of **1** with  $\text{X}_2$  under photoirradiation at room temperature (Fig. 10b). Such photoreactions are possibly triggered from the photo-induced cleavage of the Ir-Ir bond in **1** because the related reactions were not observed in the dark. Based on the

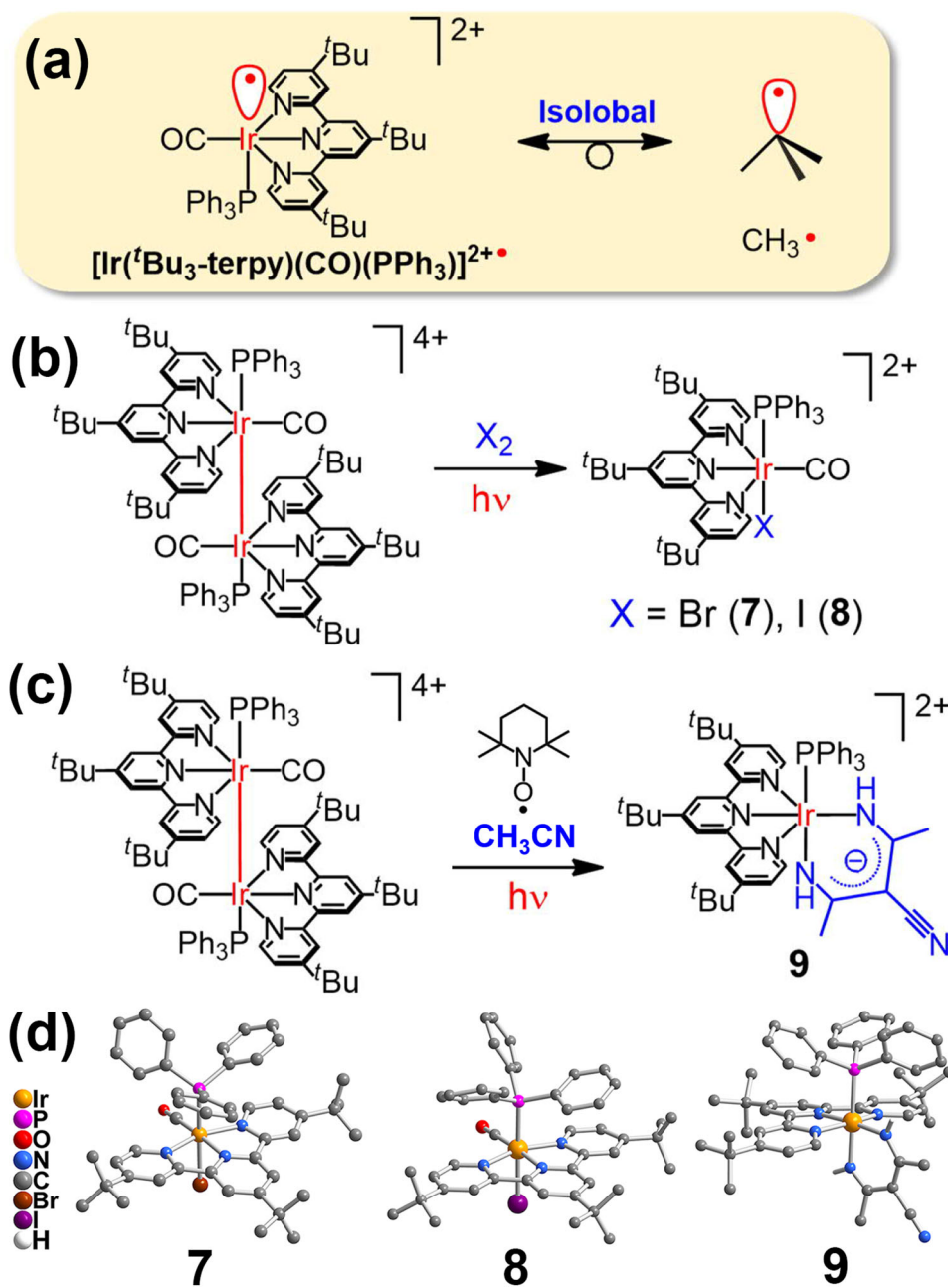


**Fig. 10** Photoreactivity of **1**. **a** Isolobal analogy of  $[\mathbf{1}_{1/2}]^{2+\bullet}$  radical. Photoreaction of **1** with  $\text{Br}_2$  or  $\text{I}_2$  (**b**); and with TEMPO (**c**) in  $\text{CH}_3\text{CN}$  solution at 298 K. The perspective drawing of molecular cations of **7–9** (**d**). Hydrogen atoms are omitted for clarity, except for the imine groups in **9**.

photoreactivity and EPR studies, generation of a reactive radical monomer is suggested for these reactions. Although the excited-state potential for the oxidation process of  $\mathbf{1}^{\text{III/II}*}$  ( $-0.45$  V vs. SCE) is comparable or sufficient for the reduction of  $\text{Br}_2$  ( $+0.47$  V) or  $\text{I}_2$  ( $+0.26$  V), the very short excited-state lifetime should unfavour this bimolecular photo-induced electron-transfer process from the  $^3\text{MMLCT}$  excited state.

Attempts have been made to trap the radical species by a common spin trapping agent, TEMPO. Surprisingly, an unprecedented complex **9**,  $[\text{Ir}(\text{tBu}_3\text{-terpy})(\text{PPh}_3)\{\text{HNC}(\text{CH}_3)_2\text{C}(\text{CN})\}]^{2+}$  (86%), was isolated from the reaction of **1** with TEMPO upon photoirradiation (Fig. 10c). Uncommon trimerization of acetonitrile is ascribed to the formation of the chelating ligand,  $\{\text{HNC}(\text{CH}_3)_2\text{C}(\text{CN})\}$ , and the proposed mechanism is suggested in Supplementary Fig. S45. It is noteworthy that this reaction

cannot occur in the dark or by replacing TEMPO with potassium *tert*-butoxide. These results indicate that this reaction should involve the photogeneration of radical monomer and could not be initiated by simple deprotonation of acetonitrile. One related example about trimethylgallium-induced trimerization of acetonitrile was also reported in the presence of halide ions at  $60^\circ\text{C}$ <sup>89</sup>. No related trapped species could be isolated from the reaction of **1** with other radical trapping reagents, butylated hydroxytoluene (BHT) and diphenylethylene (DPE). All the products **7–9** from these photoreactions were fully characterized by  $^1\text{H}$ ,  $^{13}\text{C}\{^1\text{H}\}$  and  $^{31}\text{P}\{^1\text{H}\}$  NMR spectroscopy, HRMS, IR spectroscopy and satisfactory elemental analysis (Supplementary Figs. S46–S60). Their molecular structures were also confirmed by X-ray crystallography, as shown in Fig. 10d. Their structural data, selected bond distances and angles are summarized in Supplementary Tables S21–S29.

## Conclusions

We report a series of tetracationic diiridium(II) complexes with an unsupported and long Ir(II)–Ir(II) bond for the first time. Our systematic computational study unveils that they possess the largest binding (dimerization) energy than the other related diiridium(II) complexes with the shorter metal–metal bond. Significant non-covalent London dispersion interactions were realized to overcome the considerable electrostatic repulsion between the two corresponding dicationic metal fragments. Moreover, these complexes were found to exhibit photoluminescence in both solution and solid states, as the first example of luminescent unsupported diiridium(II) system. Photoreactions, including an interesting trimerization of acetonitrile, initiated from the generation of radical monomer were also explored. Experimental and computational studies on a series of unsupported diiridium(II) complexes were investigated for the understanding of their electronic structures. Tuning of photo-physical and photoreactivity properties of these diiridium(II) complexes was achieved by changing the pincer ligands in this study. Further research for the improvement of photoluminescence efficiency or exploration of other possible photo-activated radical mediated reactions by variation of different ligands is ongoing. This work provides the first systematic study of a series of unsupported diiridium(II) system to open up an avenue for the fundamental understanding about the structural, bonding and photofunctional properties of these rare complexes.

## Method

**Experimental and computational details.** See Supplementary Methods in the Supplementary Information.

**Analytical data including  $^1\text{H}$ ,  $^{13}\text{C}\{^1\text{H}\}$  and  $^{31}\text{P}\{^1\text{H}\}$  NMR spectroscopy, HRMS, IR spectrometry.** See Figs. S1–S24 and Figs. 46–60 in the Supplementary Information.

**Computational results.** See Tables S13–S20 and Tables S30–S48 in the Supplementary Information.

**General procedures.** Unless otherwise noted, all experiments were performed under an atmosphere of nitrogen with the rigid exclusion of air and moisture using standard Schlenk or cannula techniques, or in a glovebox.

**Synthesis. Preparation of [Ir(II)( $t\text{-Bu}_3\text{-terpy}$ )(CO)(PPh $_3$ ) $_2$ ][OTf] $_4$  (1).** AgOTf (56 mg, 218  $\mu\text{mol}$ ) was added to [IrCl(CO)(PPh $_3$ ) $_2$ ] (80 mg, 102  $\mu\text{mol}$ ) in dry and degassed THF (15 mL). The mixture was allowed to stir for 1 h at room temperature, and then the filtrate was transferred in a dropwise fashion to a solution of 4,4',4''-tri-*tert*-butyl-2,2':6',2''-terpyridine (42 mg, 103  $\mu\text{mol}$ ) in THF (15 mL). The resulting solution was allowed to stir for 72 h at room temperature in the absence of light, after which, the red suspension was filtered and washed with multiple portions of tetrahydrofuran (20 mL) to give a red solid mixed with metallic Ag. The mixture was dissolved in a minimum amount of CH $_3$ CN to give a deep red solution. Recrystallization by the slow diffusion of diethyl ether to the filtrate gave 1 as red crystals (77 mg, 62%).  $^1\text{H}$  NMR (400 MHz, CD $_3$ CN, 298 K):  $\delta$  8.74 (br, 4H,  $t\text{-Bu}_3\text{-terpy}$  CH), 8.31 (br, 4H,  $t\text{-Bu}_3\text{-terpy}$  CH), 7.65 (br, 4H,  $t\text{-Bu}_3\text{-terpy}$  CH), 7.45 (t,  $J$  = 7.5 Hz, 6H, PPh $_3$  CH), 7.16 (t,  $J$  = 7.8 Hz, 12H, PPh $_3$  CH), 6.69 (m, 16H,  $t\text{-Bu}_3\text{-terpy}$  CH) and PPh $_3$  CH), 1.74 (s, 18H,  $t\text{-Bu}_3\text{-terpy}$  CH $_3$ ), 1.35 ppm (s, 36H,  $t\text{-Bu}_3\text{-terpy}$  CH $_3$ ).  $^{13}\text{C}\{^1\text{H}\}$  NMR (100 MHz, CD $_3$ CN, 298 K):  $\delta$  171.6 (CO), 169.2, 166.7, 155.8, 155.2, 152.3, 133.5, 133.4, 131.0, 130.9, 128.2, 127.7, 127.2, 124.3, 124.0, 123.8, 123.7, 120.6 (aromatic C and CH), 38.3, 36.9 (CMe $_3$ ), 31.0, 30.5 ppm (CH $_3$ ).  $^{31}\text{P}\{^1\text{H}\}$  NMR (162 MHz, CD $_3$ CN, 298 K):  $\delta$  –14.2 ppm (PPh $_3$ ). IR (KBr disk):  $\nu$  = 2060  $\text{cm}^{-1}$  ( $\nu(\text{C}\equiv\text{O})$ ), 1155  $\text{cm}^{-1}$  ( $\nu(\text{S}=\text{O})$ ). HRMS (ESI). Calcd for C $_{95}\text{H}_{100}\text{F}_9\text{Ir}_2\text{N}_6\text{O}_{11}\text{P}_2\text{S}_3$  ([M – OTf] $^+$ ):  $m/z$  2215.5197. Found:  $m/z$  2215.5212. Elemental analyses calcd for C $_{100}\text{H}_{106}\text{F}_{12}\text{Ir}_2\text{N}_8\text{O}_{14}\text{P}_2\text{S}_4$  (1-2CH $_3$ CN), found (calcd): C, 49.17 (49.09); H, 4.47 (4.37); N, 4.65 (4.58).

**Preparation of [Ir(II)( $t\text{-Bu}_3\text{-terpy}$ )(CO)(PPh $_3$ ) $_2$ ][BF $_4$ ] $_4$  (1').** This complex was prepared as red crystals from AgBF $_4$  (42 mg, 218  $\mu\text{mol}$ ), [IrCl(CO)(PPh $_3$ ) $_2$ ] (80 mg, 102  $\mu\text{mol}$ ) and 4,4',4''-tri-*tert*-butyl-2,2':6',2''-terpyridine (42 mg, 103  $\mu\text{mol}$ ) in THF using the same procedure reported for 1: yield 65 mg (60%). X-ray-quality crystals were obtained by the slow diffusion of diethyl ether to the filtrate at room temperature.  $^1\text{H}$  NMR (400 MHz, CD $_3$ CN, 298 K):  $\delta$  8.71 (br, 4H,  $t\text{-Bu}_3\text{-terpy}$  CH), 8.30 (br, 4H,  $t\text{-Bu}_3\text{-terpy}$  CH), 7.60 (br, 4H,  $t\text{-Bu}_3\text{-terpy}$  CH), 7.44 (t,  $J$  = 7.6 Hz, 6H,

PPh $_3$  CH), 7.17 (t,  $J$  = 7.6 Hz, 12H, PPh $_3$  CH), 6.71 (dd,  $J_1$  = 12.8,  $J_2$  = 6.4 Hz, 12H, PPh $_3$  CH), 6.63 (br, 4H,  $t\text{-Bu}_3\text{-terpy}$  CH), 1.73 (s, 18H,  $t\text{-Bu}_3\text{-terpy}$  CH $_3$ ), 1.35 ppm (s, 36H,  $t\text{-Bu}_3\text{-terpy}$  CH $_3$ ).  $^{13}\text{C}\{^1\text{H}\}$  NMR (100 MHz, CD $_3$ CN, 298 K):  $\delta$  171.8 (CO), 169.5, 166.9, 155.5, 155.2, 152.3, 133.4, 133.3, 131.0, 130.9, 128.0, 124.4, 124.1, 123.9 (aromatic C and CH), 38.2, 36.8 (CMe $_3$ ), 31.0, 30.5 ppm (CH $_3$ ).  $^{31}\text{P}\{^1\text{H}\}$  NMR (162 MHz, CD $_3$ CN, 298 K):  $\delta$  –13.7 ppm (PPh $_3$ ).  $^{19}\text{F}\{^1\text{H}\}$  NMR (376 MHz, CD $_3$ CN, 298 K):  $\delta$  –151.16 ppm (BF $_4^-$ ). IR (KBr disk):  $\nu$  = 2056  $\text{cm}^{-1}$  ( $\nu(\text{C}\equiv\text{O})$ ). HRMS (ESI). Calcd for C $_{92}\text{H}_{100}\text{B}_3\text{F}_4\text{Ir}_2\text{N}_6\text{O}_2\text{P}_2$  ([M – BF $_4$ ] $^+$ ):  $m/z$  2029.6724. Found:  $m/z$  2029.6755. Elemental analyses calcd for C $_{92}\text{H}_{100}\text{B}_4\text{F}_6\text{Ir}_2\text{N}_6\text{O}_2\text{P}_2$  (1'), found (calcd): C, 52.01 (52.23); H, 4.88 (4.76); N, 4.04 (3.97).

**Preparation of [Ir(II)(terpyridine)(CO)(PPh $_3$ ) $_2$ ][OTf] $_4$  (2).** AgOTf (56 mg, 218  $\mu\text{mol}$ ) was added to [IrCl(CO)(PPh $_3$ ) $_2$ ] (80 mg, 102  $\mu\text{mol}$ ) in dry and degassed CH $_3$ CN (15 mL). The mixture was allowed to stir for 1 h at room temperature, and then the filtrate was transferred in a dropwise fashion to a solution of 2,2':6',2''-terpyridine (24 mg, 103  $\mu\text{mol}$ ) in CH $_3$ CN (15 mL). The resulting solution was allowed to stir for 7 days at room temperature in the absence of light, after which, the deep brown suspension was filtered and the filtrate was concentrated to 2 mL. Recrystallization by the slow diffusion of diethyl ether to the filtrate gave 2 as leaf-shaped brown crystals (59 mg, 55%).  $^1\text{H}$  NMR (400 MHz, CD $_3$ CN, 298 K):  $\delta$  8.35 (d,  $J$  = 5.6 Hz, 4H, terpyridine CH), 8.31 (t,  $J$  = 8.2 Hz, 2H, terpyridine CH), 8.02 (t,  $J$  = 8.0 Hz, 4H, terpyridine CH), 7.90 (d,  $J$  = 8.2 Hz, 4H, terpyridine CH), 7.79 (d,  $J$  = 8.0 Hz, 4H, terpyridine CH), 7.46 (t,  $J$  = 7.5 Hz, 6H, PPh $_3$  CH), 7.38 (t,  $J$  = 6.1 Hz, 4H, terpyridine CH), 7.18 (t,  $J$  = 7.9 Hz, 12H, PPh $_3$  CH), 6.72 ppm (m, 12H, PPh $_3$  CH).  $^{13}\text{C}\{^1\text{H}\}$  NMR (100 MHz, CD $_3$ CN, 298 K):  $\delta$  173.1 (CO), 156.9, 154.1, 150.6, 143.2, 143.0, 133.9, 133.3, 133.2, 133.1, 131.2, 128.5, 127.6, 123.8, 123.5, 123.2, 123.0, 120.6 ppm (aromatic C and CH).  $^{31}\text{P}\{^1\text{H}\}$  NMR (162 MHz, CD $_3$ CN, 298 K):  $\delta$  –12.3 ppm (PPh $_3$ ). IR (KBr disk):  $\nu$  = 2060  $\text{cm}^{-1}$  ( $\nu(\text{C}\equiv\text{O})$ ), 1157  $\text{cm}^{-1}$  ( $\nu(\text{S}=\text{O})$ ). HRMS (ESI). Calcd for C $_{71}\text{H}_{52}\text{F}_9\text{Ir}_2\text{N}_6\text{O}_1\text{P}_2\text{S}_3$  ([M – OTf] $^+$ ):  $m/z$  1879.1441. Found:  $m/z$  1879.1433. Elemental analyses calcd for C $_{72}\text{H}_{56}\text{F}_{12}\text{Ir}_2\text{N}_6\text{O}_{16}\text{P}_2\text{S}_4$  (2-2H $_2$ O), found (calcd): C, 41.38 (41.90); H, 2.83 (2.73); N, 4.19 (4.07).

**Preparation of [Ir(II)(*n*-Bu $_2$ bzimb)(CO)(PPh $_3$ ) $_2$ ][OTf] $_4$  (3).** This complex was prepared as deep red crystals from AgOTf (56 mg, 218  $\mu\text{mol}$ ), [IrCl(CO)(PPh $_3$ ) $_2$ ] (80 mg, 102  $\mu\text{mol}$ ) and 2,2'-(1,3-phenylene)bis[1-butyl-1*H*-benzimidazole] (44 mg, 103  $\mu\text{mol}$ ) (*n*-Bu $_2$ bzimb) in THF using the same procedure reported for 1: yield 71 mg (58%). X-ray-quality crystals were obtained by the slow diffusion of diethyl ether to the filtrate at room temperature.  $^1\text{H}$  NMR (400 MHz, CD $_3$ CN, 298 K):  $\delta$  8.92 (t,  $J$  = 8.2 Hz, 2H, *n*-Bu $_2$ bzimb CH), 8.55 (d,  $J$  = 8.3 Hz, 4H, *n*-Bu $_2$ bzimb CH), 7.53 (d,  $J$  = 7.3 Hz, 4H, *n*-Bu $_2$ bzimb CH), 7.46 (d,  $J$  = 7.3 Hz, 4H, *n*-Bu $_2$ bzimb CH), 7.27 (m, 10H, *n*-Bu $_2$ bzimb and PPh $_3$  CH), 6.90 (m, 16H, *n*-Bu $_2$ bzimb and PPh $_3$  CH), 6.36 (dd,  $J_1$  = 12.8,  $J_2$  = 6.4 Hz, 12H, PPh $_3$  CH), 6.63 (s, 18H,  $t\text{-Bu}_3\text{-terpy}$  CH $_3$ ), 4.41 (m, 4H, NCH $_2$ CH $_2$ CH $_2$ CH $_3$ ), 4.16 (m, 4H, NCH $_2$ CH $_2$ CH $_2$ CH $_3$ ), 1.57 (m, 16H, NCH $_2$ CH $_2$ CH $_2$ CH $_3$ ), 1.12 ppm (t,  $J$  = 6.8 Hz, 12H, NCH $_2$ CH $_2$ CH $_2$ CH $_3$ ).  $^{13}\text{C}\{^1\text{H}\}$  NMR (100 MHz, CD $_3$ CN, 298 K):  $\delta$  173.0 (CO), 147.8, 145.6, 144.7, 137.9, 134.9, 133.9, 133.4, 133.3, 130.3, 130.2, 129.3, 128.5, 123.8, 123.0, 122.8, 122.5, 120.6, 116.4, 114.7 (aromatic C and CH), 47.8 (NCH $_2$ CH $_2$ CH $_2$ CH $_3$ ), 33.4 (NCH $_2$ CH $_2$ CH $_2$ CH $_3$ ), 20.5 (NCH $_2$ CH $_2$ CH $_2$ CH $_3$ ), 13.9 ppm (NCH $_2$ CH $_2$ CH $_2$ CH $_3$ ).  $^{31}\text{P}\{^1\text{H}\}$  NMR (162 MHz, CD $_3$ CN, 298 K):  $\delta$  –11.0 ppm (PPh $_3$ ). IR (KBr disk):  $\nu$  = 2035  $\text{cm}^{-1}$  ( $\nu(\text{C}\equiv\text{O})$ ), 1157  $\text{cm}^{-1}$  ( $\nu(\text{S}=\text{O})$ ). HRMS (ESI). Calcd for C $_{95}\text{H}_{88}\text{F}_9\text{Ir}_2\text{N}_{10}\text{O}_{11}\text{P}_2\text{S}_3$  ([M – OTf] $^+$ ):  $m/z$  2259.4381. Found:  $m/z$  2259.4390. Elemental analyses calcd for C $_{96}\text{H}_{88}\text{F}_{12}\text{Ir}_2\text{N}_{10}\text{O}_{14}\text{P}_2\text{S}_4$  (3), found (calcd): C, 47.68 (47.88); H, 3.86 (3.68); N, 5.80 (5.82).

**Photochemical reaction of 1. Preparation of [Ir(III)( $t\text{-Bu}_3\text{-terpy}$ )(CO)(PPh $_3$ )Br][OTf] $_2$  (7).** Bromine (7 mg, 42  $\mu\text{mol}$ ) was added to 1 (66 mg, 28  $\mu\text{mol}$ ) in dry and degassed CH $_3$ CN (15 mL). The mixture was allowed to stir for 12 h at room temperature upon irradiation of light, giving a brown solution which was then concentrated to 2 mL. Recrystallization by the slow diffusion of diethyl ether to the concentrated solution gave 7 as yellow crystals (55 mg, 78%).  $^1\text{H}$  NMR (400 MHz, CD $_3$ CN, 298 K):  $\delta$  8.89 (d,  $J$  = 6.2 Hz, 2H,  $t\text{-Bu}_3\text{-terpy}$  CH), 8.39 (s, 2H,  $t\text{-Bu}_3\text{-terpy}$  CH), 8.21 (d,  $J$  = 2.1 Hz, 2H,  $t\text{-Bu}_3\text{-terpy}$  CH), 7.62 (m, 5H,  $t\text{-Bu}_3\text{-terpy}$  and PPh $_3$  CH), 7.37 (m, 6H, PPh $_3$  CH), 7.14 (m, 6H, PPh $_3$  CH), 1.61 (s, 9H,  $t\text{-Bu}_3\text{-terpy}$  CH $_3$ ), 1.41 ppm (s, 18H,  $t\text{-Bu}_3\text{-terpy}$  CH $_3$ ).  $^{13}\text{C}\{^1\text{H}\}$  NMR (100 MHz, CD $_3$ CN, 298 K):  $\delta$  171.4 (CO), 169.5, 161.9, 161.8, 157.4, 156.8, 153.7, 134.6, 134.5, 134.2, 134.1, 131.2, 131.0, 129.0, 126.6, 125.6, 123.8, 123.5, 122.9, 120.6 (aromatic C and CH), 38.4, 37.2 (CMe $_3$ ), 30.7, 30.2 ppm (CH $_3$ ).  $^{31}\text{P}\{^1\text{H}\}$  NMR (162 MHz, CD $_3$ CN, 298 K):  $\delta$  –8.0 ppm (PPh $_3$ ). IR (KBr disk):  $\nu$  = 2102  $\text{cm}^{-1}$  ( $\nu(\text{C}\equiv\text{O})$ ), 1157  $\text{cm}^{-1}$  ( $\nu(\text{S}=\text{O})$ ). HRMS (ESI). Calcd for C $_{46}\text{H}_{50}\text{BrIrN}_3\text{OP}$  ([M – 2OTf] $^{2+}$ ):  $m/z$  481.6247. Found:  $m/z$  481.6233. Elemental analyses calcd for C $_{50}\text{H}_{53}\text{BrF}_6\text{IrN}_4\text{O}_7\text{P}_2$  (7-CH $_3$ CN), found (calcd): C, 45.97 (46.08); H, 4.22 (4.10); N, 4.09 (4.30).

**Preparation of [Ir(III)( $t\text{-Bu}_3\text{-terpy}$ )(CO)(PPh $_3$ )][OTf] $_2$  (8).** This complex was prepared as yellow crystals from iodine (11 mg, 42  $\mu\text{mol}$ ) and 1 (66 mg, 28  $\mu\text{mol}$ ) in CH $_3$ CN using the same procedure reported for 7: yield 61 mg (83%). X-ray-quality crystals were obtained by the slow diffusion of diethyl ether to the concentrated solution at room temperature.  $^1\text{H}$  NMR (400 MHz, CD $_3$ CN, 298 K):  $\delta$  8.90 (d,

$J = 6.2$  Hz, 2H,  $^4\text{Bu}_3\text{-terpy CH}$ ), 8.39 (s, 2H,  $^4\text{Bu}_3\text{-terpy CH}$ ), 8.21 (d,  $J = 2.1$  Hz, 2H,  $^4\text{Bu}_3\text{-terpy CH}$ ), 7.62 (m, 5H,  $^4\text{Bu}_3\text{-terpy}$  and  $\text{PPh}_3$  CH), 7.36 (m, 6H,  $\text{PPh}_3$  CH), 7.13 (m, 6H,  $\text{PPh}_3$  CH), 1.62 (s, 9H,  $^4\text{Bu}_3\text{-terpy CH}_3$ ), 1.41 ppm (s, 18H,  $^4\text{Bu}_3\text{-terpy CH}_3$ ).  $^{13}\text{C}\{^1\text{H}\}$  NMR (100 MHz,  $\text{CD}_3\text{CN}$ , 298 K):  $\delta$  171.1 (CO), 169.4, 162.3, 157.8, 157.0, 153.7, 134.5, 134.2, 134.1, 131.2, 131.1, 129.0, 126.6, 125.7, 123.8, 123.2, 122.6 (aromatic C and CH), 38.4, 37.2 ( $\text{CMe}_3$ ), 30.7, 30.2 ppm ( $\text{CH}_3$ ).  $^{31}\text{P}\{^1\text{H}\}$  NMR (162 MHz,  $\text{CD}_3\text{CN}$ , 298 K):  $\delta$  -9.4 ppm ( $\text{PPh}_3$ ). IR (KBr disk):  $\nu = 2112$   $\text{cm}^{-1}$  ( $\nu(\text{C}\equiv\text{O})$ ), 1155  $\text{cm}^{-1}$  ( $\nu(\text{S}=\text{O})$ ). HRMS (ESI). Calcd for  $\text{C}_{47}\text{H}_{50}\text{F}_3\text{IrIn}_3\text{O}_4\text{PS}$  ( $[\text{M}-\text{OTf}]^+$ ):  $m/z$  1160.1880. Found:  $m/z$  1160.1893. Elemental analyses calcd for  $\text{C}_{48}\text{H}_{50}\text{F}_6\text{IrIn}_3\text{O}_7\text{PS}_2$  (8), found (calcd): C, 44.00 (44.04); H, 4.01 (3.85); N, 3.12 (3.21).

#### Preparation of $[\text{Ir}(\text{III})(^4\text{Bu}_3\text{-terpy})(\text{HNC}(\text{CH}_3)\text{C}(\text{CN})\text{C}(\text{CH}_3)\text{NH})(\text{PPh}_3)]$

**[OTf]<sub>2</sub> (9).** TEMPO (13 mg, 83  $\mu\text{mol}$ ) was added to 1 (24 mg, 10  $\mu\text{mol}$ ) in dry and degassed  $\text{CH}_3\text{CN}$  (3 mL). The mixture was allowed to stir for 72 h at room temperature upon irradiation of 355 nm Xe lamp, giving a yellow solution which was then concentrated to 1 mL. Recrystallization by the slow diffusion of diethyl ether to the concentrated solution gave 9 as yellow crystals (22 mg, 86%).  $^1\text{H}$  NMR (400 MHz,  $\text{CD}_3\text{CN}$ , 298 K):  $\delta$  8.42 (d,  $J = 6.1$  Hz, 2H,  $^4\text{Bu}_3\text{-terpy CH}$ ), 8.27 (s, 2H,  $^4\text{Bu}_3\text{-terpy CH}$ ), 8.00 (d,  $J = 2.0$  Hz, 2H,  $^4\text{Bu}_3\text{-terpy CH}$ ), 7.77 (br, 1H, NH), 7.64 (dd,  $J_1 = 6.1$ ,  $J_2 = 2.1$  Hz, 22H,  $^4\text{Bu}_3\text{-terpy CH}$ ), 7.50 (m, 3H,  $\text{PPh}_3$  CH), 7.27 (m, 6H,  $\text{PPh}_3$  CH), 6.89 (m, 6H,  $\text{PPh}_3$  CH), 6.77 (br, 1H, NH), 2.57 (s, 3H,  $\text{HNC}(\text{CH}_3)$ ), 1.89 (s, 3H,  $\text{HNC}(\text{CH}_3)$ ), 1.61 (s, 9H,  $^4\text{Bu}_3\text{-terpy CH}_3$ ), 1.39 ppm (s, 18H,  $^4\text{Bu}_3\text{-terpy CH}_3$ ).  $^{13}\text{C}\{^1\text{H}\}$  NMR (100 MHz,  $\text{CD}_3\text{CN}$ , 298 K):  $\delta$  168.8, 167.9, 166.1, 165.8, 159.0, 156.6, 153.6, 134.0, 133.9, 133.7, 133.0, 130.5, 130.4, 126.9, 124.7, 124.2, 124.0, 123.7, 123.6 (aromatic C and CH,  $\text{HNC}(\text{CH}_3)\text{C}(\text{CN})\text{C}(\text{CH}_3)\text{NH}$ ), 122.1 (CN), 80.4 (CCN), 37.9, 36.8 ( $\text{CMe}_3$ ), 31.0, 30.4 ( $\text{C}(\text{CH}_3)_3$ ), 28.3, 25.9 ppm ( $\text{HNC}(\text{CH}_3)\text{C}(\text{CN})\text{C}(\text{CH}_3)\text{NH}$ ).  $^{31}\text{P}\{^1\text{H}\}$  NMR (162 MHz,  $\text{CD}_3\text{CN}$ , 298 K):  $\delta$  -16.8 ppm ( $\text{PPh}_3$ ). IR (KBr disk):  $\nu = 2191$   $\text{cm}^{-1}$  ( $\nu(\text{C}\equiv\text{N})$ ), 1157  $\text{cm}^{-1}$  ( $\nu(\text{S}=\text{O})$ ). HRMS (ESI). Calcd for  $\text{C}_{53}\text{H}_{57}\text{F}_6\text{IrN}_6\text{O}_6\text{PS}_2$  ( $[\text{M}-\text{H}]^-$ ):  $m/z$  1275.3058. Found:  $m/z$  1275.3064. Elemental analyses calcd for  $\text{C}_{53}\text{H}_{58}\text{F}_6\text{IrN}_6\text{O}_6\text{PS}_2$  (9), found (calcd): C, 49.46 (49.87); H, 4.73 (4.58); N, 6.54 (6.58).

#### Data availability

Experimental and computational details can be accessed from Supplementary Methods in the Supplementary Information. Analytical data including  $^1\text{H}$ ,  $^{13}\text{C}\{^1\text{H}\}$  and  $^{31}\text{P}\{^1\text{H}\}$  NMR spectroscopy, HRMS, IR spectrometry can be obtained from Figs. S1–S24 and Tables S13–S20 and Tables S30–S48 in the Supplementary Information. Cartesian coordinates from computational studies can be accessed from Supplementary Data 1 from this article.

The X-ray crystallographic coordinates for structures reported in this Article have been deposited at the Cambridge Crystallographic Data Centre (CCDC), under deposition number CCDC-2167632 (1), CCDC-2167633 (1<sup>†</sup>), CCDC-2167634 (2), CCDC-2167635 (3), CCDC-2167638 (7), CCDC-2167636 (8), CCDC-2167637 (9). These data can be obtained free of charge from The Cambridge Crystallographic Data Centre via [www.ccdc.cam.ac.uk/data\\_request/cif](http://www.ccdc.cam.ac.uk/data_request/cif), or accessed from Supplementary Data 2–8 from this article.

Received: 15 July 2022; Accepted: 9 November 2022;

Published online: 23 November 2022

#### References

- Hetterscheid, D. G. H. et al.  $\text{Ir}^{\text{II}}$ (ethene): metal or carbon radical? *J. Am. Chem. Soc.* **127**, 1895–1905 (2005).
- García, M. P., Jiménez, M. V., Oro, L. A., Lahoz, F. J. & Alonso, P. J. A paramagnetic, mononuclear organometallic iridium(II) complex:  $[\text{Ir}(\text{C}_6\text{Cl}_5)_2(\text{cod})]$ . *Angew. Chem. Int. Ed. Engl.* **31**, 1527–1529 (1992).
- Fuchigami, K., Rath, N. P. & Mirica, L. M. Mononuclear rhodium(II) and iridium(II) complexes supported by tetradentate pyridinophane ligands. *Inorg. Chem.* **56**, 9404–9408 (2017).
- Teets, T. S. & Nocera, D. G. Mechanistic studies of  $\text{O}_2$  reduction effected by group 9 bimetallic hydride complexes. *J. Am. Chem. Soc.* **133**, 17796–17806 (2011).
- Linck, R. C., Pafford, R. J. & Rauchfuss, T. B. Heterolytic and homolytic activation of dihydrogen at an unusual iridium (II) sulfide. *J. Am. Chem. Soc.* **123**, 8856–8857 (2001).
- Rubio-Pérez, L. et al. A bimetallic iridium(II) catalyst:  $[\{\text{Ir}(\text{IDipp})(\text{H})\}_2][\text{BF}_4]_2$  (IDipp = 1,3-bis(2,6-diisopropylphenyl)imidazol-2-ylidene). *Chem. Commun.* **51**, 9860–9863 (2015).
- Yang, W., Zhang, S., Ding, Y., Shi, L. & Song, Q. A photoluminescent dinuclear phenylquinolyl Ir(II)-Ir(II) complex featuring a  $\mu\text{-}\eta^1\text{-}\eta^2$ -phenylquinolyl bridge and an end-on dinitrogen ligand. *Chem. Commun.* **47**, 5310–5312 (2011).
- Ebihara, M., Kanematsu, N., Sakuma, T., Noritake, S. & Kawamura, T. Ligand substitution reactions of bis( $\mu$ -acetato)dichlorodicyanonyldiiridium(II). *Inorg. Chim. Acta* **358**, 2174–2182 (2005).
- Casado, M. A. et al. Stereoselective oxidative additions of iodoalkanes and activated alkynes to a sulfido-bridged heterotrimeric early-late (TiIr<sub>2</sub>) complex. *Inorg. Chem.* **42**, 3956–3964 (2003).
- Kimura, T., Ishiwata, K., Kuwata, S. & Ikariya, T. Trapping of a doubly unsaturated dinuclear iridium(II) sulfonylimido complex with phosphine and Lewis acidic group 11 and 12 metals. *Organometallics* **31**, 1204–1207 (2012).
- Tejel, C., Ciriano, M. A., López, J. A., Lahoz, F. J. & Oro, L. A. Oxidative-addition of organic monochloro derivatives to dinuclear iridium complexes: the detection of tautomeric equilibria and their implications on the reactivity. *Organometallics* **19**, 4977–4984 (2000).
- Cotton, F. A., Murillo, C. A. & Walton, R. A. *Multiple Bonds between Metal Atoms* (Springer Science and Business Media, 2005).
- Rasmussen, P. G., Anderson, J. E., Bailey, O. H., Tamres, M. & Bayon, J. C. A novel metal-metal bonded iridium(II) dimer. *J. Am. Chem. Soc.* **107**, 279–281 (1985).
- Del Rossi, K. J. & Wayland, B. B. Formation and organometallic reactivity of iridium(II) octaethylporphyrin dimer. *J. Chem. Soc. Chem. Commun.* **22**, 1653–1655 (1986).
- Hückstädt, H. & Homborg, H. Dimeric Ir<sup>II</sup>-phthalocyaninates with an Ir–Ir bond: Crystal structure of di(pyridinephthalocyaninato(2-)-iridium(II)). *Inorg. Allg. Chem.* **623**, 369–378 (1997).
- Patra, S. K., Rahaman, S. M. W., Majumdar, M., Sinha, A. & Bera, J. K. A rare unsupported iridium(II) dimer,  $[\text{IrCl}_2(\text{CO})_2]_2$ . *Chem. Commun.* **22**, 2511–2513 (2008).
- Heinekey, D. M., Fine, D. A. & Barnhart, D. Protonation of metal-metal bonds in dinuclear iridium complexes: consequences for structure and reactivity. *Organometallics* **16**, 2530–2538 (1997).
- Mak, K. H. G., Chan, P. K., Fan, W. Y., Ganguly, R. & Leong, W. K. Photochemical reaction of  $\text{Cp}^*\text{Ir}(\text{CO})_2$  with  $\text{C}_6\text{F}_5\text{X}$  (X = CN, F): Formation of diiridium(II) complexes. *Organometallics* **32**, 1053–1059 (2013).
- Huang, H., Rheingold, A. L. & Hughes, R. P. Serendipitous discovery of a simple compound with an unsupported Ir–Ir bond. *Organometallics* **28**, 1575–1578 (2009).
- Lee, H.-P. et al. A novel cyclometalated dimeric iridium complex,  $[(\text{dfpbo})_2\text{Ir}]_2$  2 [ $\text{dfpbo} = 2\text{-}(3,5\text{-Difluorophenyl})\text{benzoxazolato-N,C}^2$ ], containing an unsupported IrII–IrII bond. *Inorg. Chem.* **48**, 1263–1265 (2009).
- Einstein, F. W. B. et al. Structures of cationic di-iridium complexes derived from  $(\eta^5\text{-C}_5\text{Me}_5)\text{Ir}(\text{CO})_2$ , including the dication  $[(\eta^5\text{-C}_5\text{Me}_5)(\text{CO})_2\text{Ir}-\text{Ir}(\text{CO})_2(\eta^5\text{-C}_5\text{Me}_5)]^{2+}$  and the bridging methylenetetramethylcyclopentadienyl (tetramethylfulvene) complex  $[(\eta^5\text{-C}_5\text{Me}_5)(\text{CO})\text{Ir}-\text{Ir}(\text{CO})_2(\eta^5\text{-CH}_2\text{C}_5\text{Me}_4)]^+$ . *J. Chem. Soc. Chem. Commun.* **19**, 1424–1426 (1989).
- Heinekey, D. M., Fine, D. A., Harper, T. G. P. & Michel, S. T. Dinuclear dihydride complexes of iridium: a study of structure and dynamics. *Can. J. Chem.* **73**, 1116–1125 (1995).
- Kuo, J. L. & Goldberg, K. I. Metal/ligand proton tautomerism facilitates dinuclear  $\text{H}_2$  reductive elimination. *J. Am. Chem. Soc.* **142**, 21439–21449 (2020).
- Doyle, M. P. & Ren, T. The influence of ligands on Dirhodium(II) on reactivity and selectivity in metal carbene reactions. *Prog. Inorg. Chem.* **49**, 113–168 (2001).
- Adams, R. D. & Cotton, F. A. Eds. *Catalysis by Di- and Polynuclear Metal Cluster Complexes* (Wiley-VCH, New York, 1998).
- Doyle, M. P. & Forbes, D. C. Recent advances in asymmetric catalytic metal carbene transformations. *Chem. Rev.* **98**, 911–936 (1998).
- Doyle, M. P. Electrophilic metal carbenes as reaction intermediates in catalytic reactions. *Acc. Chem. Res.* **19**, 348–356 (1986).
- Doyle, M. P., McKervy, M. A. & Ye, T. *Modern Catalytic Methods for Organic Synthesis with Diazo Compounds: From Cyclopropanes to Ylides* (Wiley, New York, 1998).
- Xu, B., Li, M.-L., Zuo, X.-D., Zhu, S.-F. & Zhou, Q.-L. Catalytic asymmetric arylation of  $\alpha$ -aryl- $\alpha$ -diazoacetates with aniline derivatives. *J. Am. Chem. Soc.* **137**, 8700–8703 (2015).
- Guo, J.-X., Zhou, T., Xu, B., Zhu, S.-F. & Zhou, Q.-L. Enantioselective synthesis of  $\alpha$ -alkenyl  $\alpha$ -amino acids via N–H insertion reactions. *Chem. Sci.* **7**, 1104–1108 (2016).
- Cheng, Q.-Q., Yedoyan, J., Arman, H. & Doyle, M. P. Dirhodium(II)-catalyzed annulation of enoldiazoacetamides with  $\alpha$ -diazo ketones: an efficient and highly selective approach to fused and bridged ring systems. *Angew. Chem. Int. Ed.* **55**, 5573–5576 (2016).
- Deng, Y., Massey, L. A., Rodriguez Núñez, Y. A., Arman, H. & Doyle, M. P. Catalytic divergent [3+3]- and [3+2]-cycloaddition by discrimination between diazo compounds. *Angew. Chem. Int. Ed.* **56**, 12292–12296 (2017).

33. Chen, P.-A., Setthakarn, K. & May, J. A. A binaphthyl-based scaffold for a chiral dirhodium(II) biscarboxylate ligand with  $\alpha$ -quaternary carbon centers. *ACS Catal.* **7**, 6155–6161 (2017).
34. Chifotides, H. T. & Dunbar, K. R. Interactions of metal-metal-bonded antitumor active complexes with DNA fragments and DNA. *Acc. Chem. Res.* **38**, 146–156 (2005).
35. Jalilvand, F., Enriquez Garcia, A. & Niksirat, P. Reactions of antitumor active dirhodium(II) tetraacetate  $\text{Rh}_2(\text{CH}_3\text{COO})_4$  with cysteine and its derivatives. *ACS Omega* **2**, 6174–6186 (2017).
36. Li, Z. et al. Optimizing the electronic properties of photoactive anticancer oxypyridine-bridged dirhodium(II,II) complexes. *J. Am. Chem. Soc.* **136**, 17058–17070 (2014).
37. Peña, B., Barhoumi, R., Burghardt, R. C., Turro, C. & Dunbar, K. R. Confocal fluorescence microscopy studies of a fluorophore-labeled dirhodium compound: visualizing metal-metal bonded molecules in lung cancer (A549) cells. *J. Am. Chem. Soc.* **136**, 7861–7864 (2014).
38. Bradley, P. M., Bursten, B. E. & Turro, C. Excited-state properties of  $\text{Rh}_2(\text{O}_2\text{CCH}_3)_4(\text{L})_2$  ( $\text{L} = \text{CH}_3\text{OH}$ , THF,  $\text{PPh}_3$ , py). *Inorg. Chem.* **40**, 1376–1379 (2001).
39. Bradley, P. M., Fu, P. K. L. & Turro, C. Excited state properties of  $\text{Rh}_2(\text{O}_2\text{CCH}_3)_4$ : solution photochemistry and photoinitiated DNA cleavage. *Comments Inorg. Chem.* **22**, 393–426 (2001).
40. Fu, P. K. L., Bradley, P. M. & Turro, C. DNA cleavage by photogenerated  $\text{Rh}_2(\text{O}_2\text{CCH}_3)_4(\text{H}_2\text{O})^{2+}$ . *Inorg. Chem.* **40**, 2476–2477 (2001).
41. Heyduk, A. F. & Nocera, D. G. Hydrogen produced from hydrohalic acid solutions by a two-electron mixed-valence photocatalyst. *Science* **293**, 1639–1641 (2001).
42. Heyduk, A. F., Macintosh, A. M. & Nocera, D. G. Four-electron photochemistry of dirhodium fluorophosphine compounds. *J. Am. Chem. Soc.* **121**, 5023–5032 (1999).
43. Sigal, I. S., Mann, K. R. & Gray, H. B. Solar energy storage reactions. Thermal and photochemical redox reactions of polynuclear rhodium isocyanide complexes. *J. Am. Chem. Soc.* **102**, 7252–7256 (1980).
44. Esswein, A. J., Veige, A. S. & Nocera, D. G. A photocycle for hydrogen production from two-electron mixed-valence complexes. *J. Am. Chem. Soc.* **127**, 16641–16651 (2005).
45. Powers, D. C., Hwang, S. J., Zheng, S.-L. & Nocera, D. G. Halide-bridged binuclear HX-splitting catalysts. *Inorg. Chem.* **53**, 9122–9128 (2014).
46. Cotton, F. A., Lin, C. & Murillo, C. A. Supramolecular arrays based on dimetal building units. *Acc. Chem. Res.* **34**, 759–771 (2001).
47. Holliday, B. J. & Mirkin, C. A. Strategies for the construction of supramolecular compounds through coordination chemistry. *Angew. Chem. Int. Ed.* **40**, 2022–2043 (2001).
48. Cotton, F. A., Lin, C. & Murillo, C. A. The use of dimetal building blocks in convergent syntheses of large arrays. *Proc. Natl Acad. Sci. U. S. A.* **99**, 4810–4813 (2002).
49. Sun, Y. et al. Management of singlet and triplet excitons for efficient white organic light-emitting devices. *Nature* **440**, 908–912 (2006).
50. Li, T.-Y. et al. Rational design of phosphorescent iridium(III) complexes for emission color tunability and their applications in OLEDs. *Coord. Chem. Rev.* **374**, 55–92 (2018).
51. Lo, K. K.-W. Molecular design of bioorthogonal probes and imaging reagents derived from photofunctional transition metal complexes. *Acc. Chem. Res.* **53**, 32–44 (2020).
52. Yuan, Y.-J., Yu, Z.-T., Chen, D.-Q. & Zou, Z.-G. Metal-complex chromophores for solar hydrogen generation. *Chem. Soc. Rev.* **46**, 603–631 (2017).
53. Wong, K. M.-C., Au, V. K.-M. & Yam, V. W.-W. In *Comprehensive Inorganic Chemistry II* 2nd edn, Vol. 8 (ed. Yam, V. W.-W. et al.) 59–130 (Elsevier, 2013).
54. Zláliš, S., Hunter, B. M., Gray, H. B. & Vlček, A. Electronic structures of reduced and superreduced  $\text{Ir}_2(1,8\text{-diisocyanomethane})_4^{n+}$  complexes. *Inorg. Chem.* **56**, 2874–2883 (2017).
55. Zhao, Y. & Truhlar, D. G. A new local density functional for main-group thermochemistry, transition metal bonding, thermochemical kinetics, and noncovalent interactions. *J. Chem. Phys.* **125**, 194101 (2006).
56. Zhao, Y. & Truhlar, D. G. The M06 suite of density functionals for main group thermochemistry, thermochemical kinetics, noncovalent interactions, excited states, and transition elements: two new functionals and systematic testing of four M06-class functionals and 12 other functionals. *Theor. Chem. Acc.* **120**, 215–241 (2008).
57. Lee, C., Yang, W. & Parr, R. G. Development of the Colle-Salvetti correlation-energy formula into a functional of the electron density. *Phys. Rev. B* **37**, 785–789 (1988).
58. Becke, A. D. Density-functional thermochemistry. III. *Role Exact. Exch. J. Chem. Phys.* **98**, 5648–5652 (1993).
59. Adamo, C. & Barone, V. Toward reliable density functional methods without adjustable parameters: The PBE0 model. *J. Chem. Phys.* **110**, 6158–6170 (1999).
60. Yu, H. S., He, X., Li, S. L. & Truhlar, D. G. MN15: A Kohn–Sham global-hybrid exchange–correlation density functional with broad accuracy for multi-reference and single-reference systems and noncovalent interactions. *Chem. Sci.* **7**, 5032–5051 (2016).
61. Grimme, S., Antony, J., Ehrlich, S. & Krieg, H. A consistent and accurate ab initio parametrization of density functional dispersion correction (DFT-D) for the 94 elements H–Pu. *J. Chem. Phys.* **132**, 154104 (2010).
62. Riplinger, C., Pinski, P., Becker, U., Valeev, E. F. & Neese, F. Sparse maps—a systematic infrastructure for reduced-scaling electronic structure methods. II. Linear scaling domain based pair natural orbital coupled cluster theory. *J. Chem. Phys.* **144**, 024109 (2016).
63. Dann, T., Roşca, D.-A., Wright, J. A., Wildgoose, G. G. & Bochmann, M. Electrochemistry of  $\text{Au}^{\text{II}}$  and  $\text{Au}^{\text{III}}$  pincer complexes: determination of the  $\text{Au}^{\text{II}}\text{–Au}^{\text{III}}$  bond energy. *Chem. Commun.* **49**, 10169–10171 (2013).
64. Inoki, D., Matsumoto, T., Nakai, H. & Ogo, S. Experimental study of reductive elimination of  $\text{H}_2$  from rhodium hydride species. *Organometallics* **31**, 2996–3001 (2012).
65. Wu, L.-C. et al. Bond characterization on a Cr–Cr quintuple bond: a combined experimental and theoretical study. *J. Phys. Chem. A* **115**, 12602–12615 (2011).
66. Macchi, P., Proserpio, D. M. & Sironi, A. experimental electron density in a transition metal dimer: metal–metal and metal–ligand bonds. *J. Am. Chem. Soc.* **120**, 13429–13435 (1998).
67. Niskanen, M., Hirva, P. & Haukka, M. Computational DFT study of ruthenium tetracarbonyl polymer. *J. Chem. Theory Comput.* **5**, 1084–1090 (2009).
68. Van der Maelen, J. F. & Cabeza, J. A. QTAIM analysis of the bonding in Mo–Mo bonded dimolybdenum complexes. *Inorg. Chem.* **51**, 7384–7391 (2012).
69. Lepetit, C., Fau, P., Fajewerg, K., Kahn, M. L. & Silvi, B. Topological analysis of the metal–metal bond: a tutorial review. *Coord. Chem. Rev.* **345**, 150–181 (2017).
70. Bickelhaupt, F. M. & Houk, K. N. Analyzing reaction rates with the distortion/interaction-activation strain model. *Angew. Chem. Int. Ed.* **56**, 10070–10086 (2017).
71. Johnson, E. R. et al. Revealing noncovalent interactions. *J. Am. Chem. Soc.* **132**, 6498–6506 (2010).
72. Bader, R. F. W. *Atoms in Molecules: A Quantum Theory* (Clarendon Press, Oxford, U.K., 1990).
73. Keith, T. A. *AIMAll (Version 19.10.12), TK Gristmill Software* (Overland Park KS, USA, 2019).
74. Wagner, J. P. & Schreiner, P. R. London dispersion in molecular chemistry—reconsidering steric effects. *Angew. Chem. Int. Ed.* **54**, 12274–12296 (2015).
75. Liprot, D. J. & Power, P. P. London dispersion forces in sterically crowded inorganic and organometallic molecules. *Nat. Rev. Chem.* **1**, 0004 (2017).
76. Lu, Q., Neese, F. & Bistoni, G. Formation of agostic structures driven by London dispersion. *Angew. Chem. Int. Ed.* **57**, 4760–4764 (2018).
77. Koby, R. F., Hanusa, T. P. & Schley, N. D. Mechanochemically driven transformations in organotin chemistry: stereochemical rearrangement, redox behavior, and dispersion-stabilized complexes. *J. Am. Chem. Soc.* **140**, 15934–15942 (2018).
78. Liprot, D. J., Guo, J.-D., Nagase, S. & Power, P. P. Dispersion forces, disproportionation, and stable high-valent late transition metal alkyls. *Angew. Chem. Int. Ed.* **55**, 14766–14769 (2016).
79. Grimme, S. & Djukic, J.-P. Cation–cation “attraction”: when London dispersion attraction wins over coulomb repulsion. *Inorg. Chem.* **50**, 2619–2628 (2011).
80. Bursch, M. et al. Understanding and quantifying London dispersion effects in organometallic complexes. *Acc. Chem. Res.* **52**, 258–266 (2019).
81. Wan, Q., Yang, J., To, W.-P. & Che, C.-M. Strong metal–metal Pauli repulsion leads to repulsive metallophilicity in closed-shell  $d^8$  and  $d^{10}$  organometallic complexes. *Proc. Natl Acad. Sci. USA* **118**, e2019265118 (2021).
82. Zeng, J., Zhao, Y., Xu, F. & Zhu, J. Probing hyperconjugative aromaticity in 2H-pyrrolium and cyclopentadiene containing group 9 transition metal substituents: bridged carbonyl ligands can enhance aromaticity. *Phys. Chem. Chem. Phys.* **23**, 2697–2702 (2021).
83. Runge, E. & Gross, E. K. U. Density-functional theory for time-dependent systems. *Phys. Rev. Lett.* **52**, 997–1000 (1984).
84. de Souza, B., Farias, G., Neese, F. & Izsák, R. Predicting phosphorescence rates of light organic molecules using time-dependent density functional theory and the path integral approach to dynamics. *J. Chem. Theory Comput.* **15**, 1896–1904 (2019).
85. Mai, S. et al. Quantitative wave function analysis for excited states of transition metal complexes. *Coord. Chem. Rev.* **361**, 74–97 (2018).
86. Harvey, J. N., Aschi, M., Schwarz, H. & Koch, W. The singlet and triplet states of phenyl cation. A hybrid approach for locating minimum energy crossing points between non-interacting potential energy surfaces. *Theor. Chem. Acc.* **99**, 95–99 (1998).
87. Alonso, P. J. et al. Synthesis of tetranuclear rhodium and iridium complexes directed by 6-mercaptopyridin-2-ol: electrochemical behavior, chemical oxidation, and coordination chemistry. *Inorg. Chem.* **48**, 7984–7993 (2009).

88. De Bruin, B., Hetterscheid, D. G. H., Koekkoek, A. J. J. & Grützmacher, H. The organometallic chemistry of Rh-, Ir-, Pd-, and Pt-based radicals: higher valent species. *Prog. Inorg. Chem.* <https://doi.org/10.1002/9780470144428.ch5> (2007).
89. Kopp, M. R., Kräuter, T., Dashti-Mommertz, A. & Neumüller, B. Trimethylgallium-induced trimerization of acetonitrile. *Organometallics* **17**, 4226–4231 (1998).

### Acknowledgements

K.M.-C.W. acknowledges the National Natural Science Foundation of China (22171126), the Science, Technology and Innovation Commission of Shenzhen Municipality (JCYJ20210324104609025 and JCYJ20190809165411528), and the assistance of SUSTech Core Research Facilities. We gratefully thank Dr. Z. Tang, Dr. Y.H. Yang and Mr. N. Qin for their help and discussions in EPR measurements. L.W.C. acknowledges the National Natural Science Foundation of China (21933003, 22193020 and 22193023), Shenzhen Nobel Prize Scientists Laboratory Project (CI7783101) and Guangdong Provincial Key Laboratory of Catalysis (2020B121201002) as well as the Center for Computational Science and Engineering at SUSTech and the CHEM high performance supercomputer cluster at department of chemistry, SUSTech.

### Author contributions

K.M.-C.W. directed and conceived this project. F.Z., S.W., S.Z., Y.Z., H.S. and J.-F.D. conducted the experiments. Y.Y., Z.Y. and L.W.C. did the theoretical works. All authors discussed the results and wrote the manuscript. L.W.C. and K.M.-C.W. performed data analysis and prepared the manuscript. All authors have given approval to the final version of the manuscript.

### Competing interests

The authors declare no competing interests.

### Additional information

**Supplementary information** The online version contains supplementary material available at <https://doi.org/10.1038/s42004-022-00775-4>.

**Correspondence** and requests for materials should be addressed to Lung Wa Chung or Keith Man-Chung Wong.

**Peer review information** *Communications Chemistry* thanks Congqing Zhu and the other, anonymous, reviewer(s) for their contribution to the peer review of this work. Peer reviewer reports are available.

**Reprints and permission information** is available at <http://www.nature.com/reprints>

**Publisher's note** Springer Nature remains neutral with regard to jurisdictional claims in published maps and institutional affiliations.



**Open Access** This article is licensed under a Creative Commons Attribution 4.0 International License, which permits use, sharing, adaptation, distribution and reproduction in any medium or format, as long as you give appropriate credit to the original author(s) and the source, provide a link to the Creative Commons license, and indicate if changes were made. The images or other third party material in this article are included in the article's Creative Commons license, unless indicated otherwise in a credit line to the material. If material is not included in the article's Creative Commons license and your intended use is not permitted by statutory regulation or exceeds the permitted use, you will need to obtain permission directly from the copyright holder. To view a copy of this license, visit <http://creativecommons.org/licenses/by/4.0/>.

© The Author(s) 2022